DESIGN OF AN IRRADIATION TEST FACILITY FOR SPACE APPLICATIONS

A THESIS SUBMITTED TO
THE GRADUATE SCHOOL OF NATURAL AND APPLIED SCIENCES
OF
MIDDLE EAST TECHNICAL UNIVERSITY

BY

DİLEK KIZILÖREN

IN PARTIAL FULFILLMENT OF THE REQUIREMENTS
FOR
THE DEGREE OF MASTER OF SCIENCE
IN
PHYSICS

FEBRUARY 2014

Approval of the thesis:

DESIGN OF AN IRRADIATION TEST FACILITY FOR SPACE APPLICATIONS

submitted by **DİLEK KIZILÖREN** in partial fulfillment of the requirements for the degree of **Master of Science in Physics Department, Middle East Technical University** by,

Prof. Dr. Canan Özgen
Dean, Graduate School of **Natural and Applied Sciences**   ——————————

Prof. Dr. Mehmet Zeyrek
Head of Department, **Physics**   ——————————

Assoc. Prof. Dr. Bilge Demirköz
Supervisor, **Physics Department, METU**   ——————————

Examining Committee Members:

Prof. Dr. Mehmet Zeyrek
Physics Department, METU   ——————————

Assoc. Prof. Dr. Bilge Demirköz
Physics Department, METU   ——————————

Prof. Dr. Altuğ Özpineci
Physics Department, METU   ——————————

Assoc. Prof. Dr. Serhat Çakır
Physics Department, METU   ——————————

Dr. Alime Yanartaş Özyıldırım
ASELSAN   ——————————

                     Date: ——————————

I hereby declare that all information in this document has been obtained and presented in accordance with academic rules and ethical conduct. I also declare that, as required by these rules and conduct, I have fully cited and referenced all material and results that are not original to this work.

Name, Last Name: DİLEK KIZILÖREN

Signature   :

ABSTRACT

DESIGN OF AN IRRADIATION TEST FACILITY FOR SPACE APPLICATIONS

Kızılören, Dilek

M.S., Department of Physics

Supervisor   : Assoc. Prof. Dr. Bilge Demirköz

February 2014, 51 pages

Space radiation damages electronic components of spacecraft. Damages are due to cosmic rays which consist of protons, photons, electrons, and heavy nuclei. Functionality and performance of the electronic components in flight depend on the orbital parameters of spacecrafts and exposure time. The space radiation causes three types of effects and these are categorized as Single Event Effects (SEEs), Total Ionizing Dose (TID) Effects and Non-Ionizing Dose Displacement Damage Effects. Radiation hardness assurance tests have to be conducted to ensure performance and functionality during operational lifetime of spacecraft.

SEE radiation tests are planned to be carried out using a 30 MeV beam line in the Research and Development room of Turkish Atomic Energy Agency (TAEK) at Sarayköy Nuclear Research and Training Center (SANAEM). A reduction of the flux and an enlargement of the target irradiation area are necessary to perform tests according to ESA Standards. Collimator and thin films are planned to be used to expand the beam line and reduce the flux. The simulation of beam line design is carried out using FLUKA and MADX. The first SEEs radiation test in Turkey is foreseen to be carried out using this beam line.

Keywords: Space radiation environment, interaction of particles with matter, single event effects, MADX, FLUKA

ÖZ

UZAY UYGULAMALARI İÇİN RADYASYON TEST TESİSİ TASARIMI

Kızılören, Dilek

Yüksek Lisans, Fizik Bölümü

Tez Yöneticisi   : Doç. Dr. Bilge Demirköz

Şubat 2014 , 51 sayfa

Uzay radyasyonu uydu araçlarının elektronik bileşenlerine zarar vermektedir. Bu zarar protonlar, fotonlar, elektronlar ve ağır çekirdeklerden oluşan kozmik ışınlardan meydana gelmektedir. Uzay araçlarının elektronik parçalarının verimliliği ve işlevselliği uzay aracının yörünge parametrelerine ve maruz kalınan zamana ve bağlıdır. Uzay radyasyonu iki çeşit etkiye sebep olur ve bunlar Tekil Olay Etkileri, Toplam İyonlaşma Doz (TID) etkisi ve İyonize Olmamış Doz Etkiyen Yer Değiştirme Hasarı olmak üzere sınıflandırılırlar. Bu sebeple radyasyona dayanıklılık testi, uzay aracının çalışma süresi boyunca verimliliğinin ve işlevselliğinin güvence altına alınması için zorunludur

Tek olay etkileri radyasyon testleri 30 MeV demet hattına sahip Türkiye Atom Enerjisi Kurumu (TAEK)'nun Sarayköy Nükleer Araştırma ve Eğitim Merkezi'nde (SANAEM) bulunan Araştırma ve Geliştirme (ArGe) odasında gerçekleştirilmesi planlanmaktadır. Akının düşürülmesi ve hedefin radyasyona maruz kaldığı alanın genişletilmesi ESA Standartlarına göre gereklidir. Kolimatör ve ince filmler demetin genişletilmesi ve akının düşürülmesi için kullanılmaktadır. Demet hattının simülasyonunda FLUKA ve MADX programları kullanılmaktadır. Bu demet hattı kullanılarak Türkiye'de ilk Tekil Olay Etkileri testlerinin gerçekleştirileceği öngörülmektedir.

Anahtar Kelimeler: Uzay radyasyon ortamı, madde ile etkileşim, tek olay etkileri, MADX, FLUKA

vii

To my family

ACKNOWLEDGMENTS

TABLE OF CONTENTS

LIST OF TABLES

LIST OF FIGURES

FIGURES

LIST OF ABBREVIATIONS

AMS	Alpha Magnetic Spectrometer
eV	Electron Volt
GEO	Geostationary and Geosynchronous
HEO	High Earth Orbit
LET	Linear Energy Transfer
LEO	Low Earth Orbit
MEO	Medium Earth Orbit
PAF	Proton Accelerator Facility
SAA	South Atlantic Anomaly
SANAEM	Sarayköy Nuclear Research And Training Center
SEB	Single Event Burnout
SEE	Single Event Effect
SEL	Single Event Latch-up
SEU	Single Event Upset
TID	Total Ionizing Dose
TAEK	Turkish Atomic Energy Agency

CHAPTER 1

INTRODUCTION

This thesis addresses three related topics:

1. The effects of trapped particles, solar cycle, orbit parameters of spacecrafts on electronic components of satellites.

2. An understanding of the interaction of particles with matter.

3. Expansion of TAEK Proton Accelerator Facility(PAF) beam line to use SEE radiation test for large target area.

Performance and functionality of electronic components of satellites can change due to exposure to radiation in space. The radiation dose received depends on the types of particles, the trapped flux in Earth's magnetic field and the primary flux which falls exponentially with particle energy above the geomagnetic cutoff. The flux of charged particles change with respect to altitude and position due to the Earth's magnetic field resulting in Van Allen Belts and also during solar events. All of these lead to damage during the operational time. While a long term exposure to radiation leads to total dose effects, ionization of single particles cause single event errors. Today, as technology develops, electronic component are getting smaller and more complex. As seen in Figure 1.1, single event errors become more important than total dose effects. While size of electronic components are getting smaller, their operational voltage decreases, as a result of this, probability of single event errors increase [9]. As the oxide in transistor is getting thinner and oxide/silicon interfaces improve, total ionizing dose effects reduce. Radiation hardness tests are important in preparing the electronic components of satellites for radiation and guaranteeing their performance.
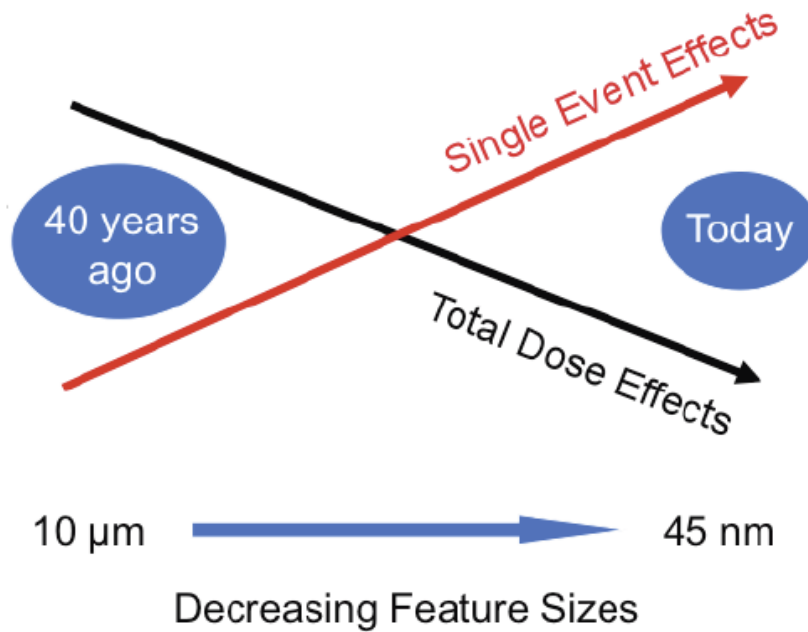
Figure 1.1: Single Event Errors increase as electronic component get smaller[9].

Generally, the purpose of radiation hardness testing is to assure the resistance of electronic components in the natural space radiation environment. Institutes in Europe and the USA have developed international standards for qualifying electronic devices under operating radiation. ESA/SCC and ECSS Specifications (Europe) and MIL-STD Specifications (USA) can be given as examples [11]. These standards describe the basic requirements for testing of electronic components.

SEE radiation test procedure, specified in ESA/SCC Single Event Effects Test Method and Guidelines Basic Specification No. 25100, defines properties of usable radiation sources and test procedures. When TAEK Proton Accelerator Facility(PAF) properties are compared with this standard, it can be observed that the cyclotron has a high flux value and a small test area. As shown in Table 1.1, quadrupole magnets must be employed to enlarge the beam and decrease the flux, collimator and thin Cu films must be used so that the SEE radiation tests can be perform without extra damage to target.

In this thesis, a design for SEE radiation test according to the test standard is described. First of all, many simulations have been performed to find the proper thickness of thin films to decrease the fluence. Although the particles hit the films, sec-

Table 1.1: Irradiation Conditions according to ESA/SCC 25100 Standard and TAEK Proton Accelerator Facility(PAF) Properties

ESA/SCC 25100 Standard	Properties of TAEK PAF
Energy Range: 20-200 MeV	Energy of PAF: 30 MeV
Flux Range: $10^5 >$ flux $> 10^8$ $p{\cdot}cm^{-2}{\cdot}s^{-1}$	Flux of PAF: 10^{11} $p{\cdot}cm^{-2}{\cdot}s^{-1}$

ondary particles emerge due to scattering. To eliminate secondary particles and also to decrease flux by eliminating number of particles, collimator system is used. Two thin films, before the collimator design, are presented in Chapter 3.

In Chapter 2, space radiation environment, interaction with matter and space radiation effects are described. Space radiation effects, Single Event Effects (SEEs), Total Ionizing Dose (TID) and Non-Ionizing Dose Displacement Damage Effects are explained. In Chapter 3, the design of a radiation test laboratory for SEEs is shown. The beam line properties are also discussed in this chapter and a conclusion is given in Chapter 4.

CHAPTER 2

SPACE RADIATION ENVIRONMENT AND EFFECTS

2.1   Introduction

Electronic components of spacecraft are exposed to a wide range of space radiation. The space environment consists of particles coming from the Sun, trapped particles in Van Allen radiation belts and galactic cosmic rays. In order to use electronics components reliably in space, radiation effects have to be understood thoroughly.

Since the start of the space age, space radiation environment has posed a very serious problem for spacecraft. Radiation effects have caused one or two total or partial mission loss per year over the past 20 years [31]. In 2003, during Halloween Storms the Solar and Heliospheric Observatory (SOHO) satellite failed temporarily. In the same year, NASA's Advance Composition Explorer (ACE) satellite was damaged and several spacecraft had to be shut down temporarily [16]. Cosmic rays affect not only satellites, but also planes. For example, in 2009, Qantas Flight experienced a drop in altitude over Western Australia because of a computer error [37]. Figure 2.1 shows the flight computer that failed on the right, damage to flight equipment due to dropping altitude. 11 passengers were seriously injured.

Therefore, it is important to understand what kind of effects could be encountered and how to solve them if necessary. The solution lies with the hardness assurance tests which help prepare the electronic components for space radiation. In this chapter, the space radiation environment, its effects and interaction with matter are discussed in detail.

Figure 2.1: Damage of Qantas Flight(left), Air Data Inertial Reference Unit(right).

2.2 Cosmic Rays

In 1910, Theodor Wulf made a sensitive electroscope to compare its discharging time at different altitudes. The electroscope lost its charge slowly, after it was charged. At that time, it was thought that this radiation came from Earth. If the radiation had come from the Earth, the discharging time of the electroscope at reduced Earth altitude would have been smaller than its discharging time at high altitudes. When he compared the discharging time at an underground location with that at top of the Eiffel Tower, he found that it was greater at the underground level. He concluded that the hypothesis was wrong and that the radiation did not come from Earth itself, but probably from above the atmosphere [26]. As seen in Figure 2.2, in 1911 and 1912, Victor Hess made a series of balloon experiments to understand the source of the ionization radiation [26]. In April 1912, according to his flight during a solar eclipse, he discovered that particles from Sun could not be the radiation source. He established that at high altitudes, the effect was stronger than near the ground, concluding that the effect was due to radiation from space. In August of the same year, he found that the radiation level began to increase at above 2000 m and as altitude increased, radiation level continued to rise. Thus, Victor Hess had discovered cosmic rays, which is the consequence of high energy particles. His experiments also showed that the source of radiation was extraterrestrial.

In 1925, the radiation was named "cosmic rays" by Robert A. Millikan. While investigating the Compton effect in 1927, Dmitri Vladimirovich Skobeltsyn observed the

Figure 2.2: In 1912, Victor Hess discovered cosmic rays after balloon flight, after many series balloon flights he discovered cosmic rays [26].

tracks of the particles arriving in the cloud chamber from the atmosphere. Among the tracks, he noted that some of them were deflected whereas some of them did not curve at all in the presence of a magnetic field, indicating energies in excess of 15 MeV. Although his interpretation was not correct, it was, as can be seen in Figure 2.3, the first observation of a cosmic-ray shower phenomenon [26]. He demonstrated that these particles often appear in a cloud chamber as groups of a few particles.

In 1919, Geiger-Müller detector enabled detecting individual cosmic rays. This detector was composed of a conducting hollow cylinder with a high voltage wire along its axis. The Geiger counter allowed for a very fast response time to identify the arrival time of cosmic ray events accurately, but suffered from background contamination. In 1929, Bothe and Kolhörster by using two Geiger-Müller detectors, could test whether the cosmic radiation consisted of charged particles or high energy γ-rays, which have no electrical charge. They placed 4 cm thick lead and gold slice as an absorbing slab between two Geiger-Müller detectors and they measured the number of coincidences with and without the slab. Coincidence could not be produced by γ-radiation because secondary electrons would have stopped in the absorber. Experiment showed that cosmic radiation consisted of charged particles with energies around $10^9 - 10^{10}$ eV [24, 26].

Figure 2.3: In 1929, First photographic record of cosmic rays was taken by Skobelt-syn. The track of the particle is shown by two white and one black arrows in cloud chamber [26].

Until 1953, many new particles were discovered in cosmic rays. Pierre Auger and his collaborators discovered secondary particles which were produced by cosmic rays in 1936 [21]. Studying cosmic rays and their secondary products provided the discovery of particles like positrons, pions and muons. In 1949, Enrico Fermi proposed a theory on the origin of cosmic rays. According to his theory, cosmic rays were accelerated by collisions against moving magnetic fields [23]. Around 1953, developing accelerator technology provided a way to produce new particles in a laboratory environment. Today, scientists are trying to understand the effects of cosmic ray by using accelerators. As well as balloon and space experiments, cosmic rays observations are still carried out to find out more about the space radiation environment.

Currently, the energy spectrum of cosmic ray particles can be described as

$$N(E)dE \propto E^{-\gamma}d(E) \tag{2.1}$$

where γ is called spectral index of flux and E is the particle's kinetic energy. Energy

flux is described as energy transferred from the source through a unit area per steradian per second. It is given in terms of $J \cdot m^{-2} s^{-1}$. Equation 2.1 is applicable for protons, electrons and nuclei with energy range $10^9 - 10^{14}$ eV [26].
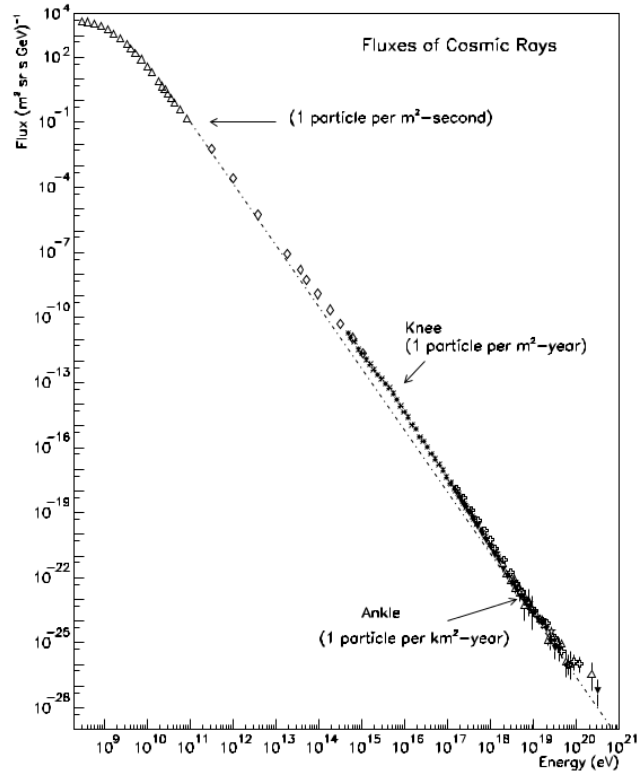
Figure 2.4: Spectrum of all particles of cosmic rays [33].

Figure 2.4 shows that total flux rate of cosmic rays with respect to their energies. According to the figure, particles with high energies have low flux rates and also cosmic ray spectrum spreads from high flux with a few MeV to around 100 GeV with low flux. *Knee* is the first kink at around 10^{15} eV and the second kink is at around 6×10^{18} eV is named as *ankle*. Today the spectrum can be observed by various experiments which depend on energy range and flux, such as satellites LEAP [30] and Proton [6], air fluorescence Fly's Eye [4], HiRes1 mono [24], and HiRes2 mono [24].

Low Earth Orbit (LEO) is a circular orbit with an altitude between 160 kilometers and 2000 kilometers. Orbital period changes from 90 minutes to 2 hours. LEO is used for military, observation and satellite phone. Most satellites such as the Hubble Space Telescope [28], the International Space Station [29] and AMS-02 [22] are in

LEO. For example, Göktürk-2 [35] was placed into a LEO polar orbit of 638 km. Any orbit around the Earth's poles is referred to as a polar orbit. Medium Earth Orbit (MEO) exists above LEO altitude from 2000 km to 35.786 km. Weather satellites, spy satellites and observation satellites are placed in MEO. Any Geostationary and Geosynchronous (GEO) orbit is usually used for television satellites, long distance communication satellites, internet, Global Positioning System (GPS). The orbital period of these satellites the same is as the rotation period of the Earth. High Earth Orbit (HEO) is defined as outside the atmosphere and the Earth. It is used for weather and space observation. Fundamental radiation sources in LEO are energetic protons and electrons trapped in the Earth's magnetic field and particles produced during solar activity.

As mentioned before, understanding the properties of the particles in radiation belts and solar activity are important to assure performance and functionality of electronic components of satellite in different orbits.

2.2.1   Trapped Particles Due To Earth's Magnetic Field

Cosmic radiation can be captured and trapped by the Earth's magnetic field. Earth's magnetic field can be approximated as a dipole magnet with a north and south pole. The center of the magnetic dipole is located at the Earth's center [17]. Equation 2.2 represents the Earth's magnetic dipole where $\mathbf{M}$ is the dipole moment ($\mathbf{M} \simeq 8.1 \times 10^{22}$ amp-meter) and $\mathbf{r}$, a radius vector from the dipole to the point in question.

$$\mathbf{H} = -grad(\mathbf{M} \cdot \mathbf{r}/4\pi r^3) \tag{2.2}$$

The Earth is accepted to be uniformly magnetized along its dipole axis. One end of the dipole axis points lies on the Earth's surface at latitude 78.5° S and longitude 111° E. This point is called the geomagnetic south pole while the point at 78.5° N and 69° W is the known as the geomagnetic north pole. The geomagnetic axis is defined as the line that joins these poles together. As can be seen Figure 2.5 geomagnetic axis is titled by 11.5°. Geomagnetic coordinates can be defined by using these polar points. The geomagnetic longitude is taken as an increasing point from 0° to 360°

which moves eastward from the zero meridian. The zero meridian starts with the south geographic pole [17].
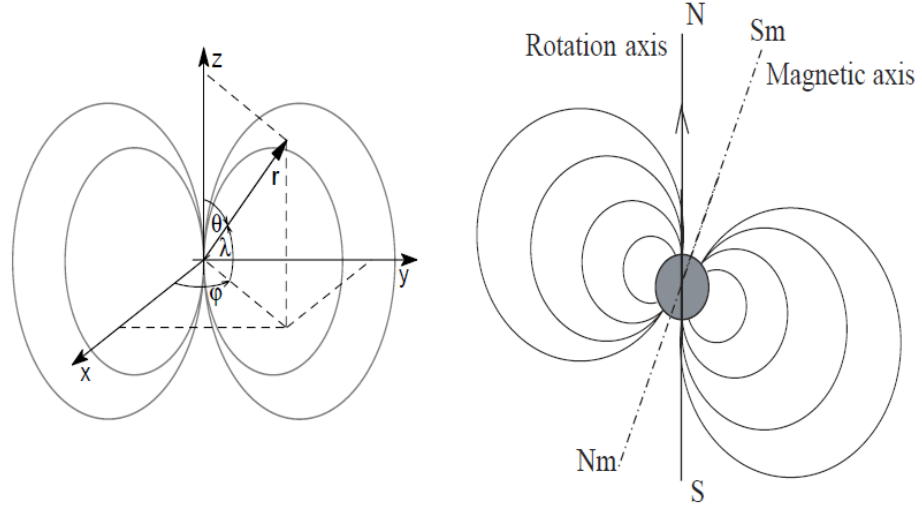
Figure 2.5: Left figure represents the coordinate axis for dipole field, the right one is magnetic axis inclination. There is 11.5° difference between geomagnetic location of poles and geographic location of poles [13].

Charged particles arrive at the Earth's magnetosphere as a function of geomagnetic latitude [26]. Magnetosphere is a region around the Earth which is created by Earth's magnetic field. The λ which represents geomagnetic latitude, can be measured with respect to the equatorial plane of the Earth's magnetic field. Using the geomagnetic latitude definition, permitted regions and forbidden zones for the particles incoming towards the Earth's surface can be defined. Equation of motion for these charged particles can be written according to Störmer Theory for the energetic ions in the magnetic dipole field [26].

$$2b = -r\sin\theta\cos\lambda - \frac{\cos^2\lambda}{r} \tag{2.3}$$

Equation 2.3 represents the motion of charged particles in the Earth's magnetic field. In this equation, r is the distance from the dipole and λ is the magnetic latitude. The range of θ angles where particles can reach the Earth's surface can be determined as a function of geomagnetic latitude, charge and momentum. If particles arrive at the

Table 2.1: Example of geomagnetic cutoff energies for protons at different geomagnetic latitudes

Geomagnetic Latitude	Momentum	Kinetic Energy
$\lambda = 0°$	p$\geq 14.9 GeV/c$	14.0 GeV
$\lambda = 40°$	p$\geq 5.1 GeV/c$	4.3 GeV
$\lambda = 60°$	p$\geq 0.93 GeV/c$	0.48 GeV

surface vertically, the value of θ is zero. Equation 2.3 becomes

$$2b = -\frac{\cos^2\lambda}{r} \qquad (2.4)$$

For particles arriving at the Earth's magnetic field

$$-\frac{1}{2}\frac{\cos^2\lambda}{(p/59.6zGeV)^{1/2}} \geq -1 \qquad (2.5)$$

Equation 2.5 shows the charged particles with momenta less than 59.6 GeV and the collision parameter b, greater than -1 satisfies this condition and can reach the Earth's atmosphere [26]. Particles with momenta greater than this value can reach the Earth's atmosphere. Equation 2.5 can be written as

$$p \geq 14.9z\cos^4\lambda GeVc^{-1} \qquad (2.6)$$

These critical values are known as the *"geomagnetic cutoff"* for particles arriving in the magnetosphere. Table 2.1 shows example critical cutoff energies to arrive in the atmosphere according to Equation 2.6.

These cutoff values can be written for different latitudes according to kinetic energy of the incoming particles. Cutoff kinetic energies range from 10 MeV to 10 GeV depending on altitude and longitude. For particles with energies between 10 and

100 GeV, the spectrum drops off in accordance with a power law above the cutoff. The flux as function of kinetic energy for downward and upward protons for different geomagnetic latitudes [1] are shown Figure 2.6 from AMS-01 experiment. The result is shown in accordance with geomagnetic latitude regions $|\theta_M|$.

Alpha Magnetic Spectrometer(AMS-01) flew on the shuttle in June 1998 and docked with space station MIR. During its 9 days of mission, it took cosmic ray data with $|\theta_M|$ ranges from 0.2 rad to 1 rad due to MIR's orbit [20]. In the figure 2.6, down-going (a,b,c) and up-going (d,e,f) proton spectrum can be seen as a function of kinetic energies. High energy down going protons which come to the equatorial region with different trajectories overcome the cutoff and enter the Earth's atmosphere. On the other hand, lower energy protons slide to the poles and they can remain trapped for a long time. The spectrum below the cutoff region represents evidence for trapped particles in the Earth's magnetic field: down-going and up-going protons spectra are observed to be similar. Separation between primary and secondary spectrum (trapped spectrum) can be seen above this point [13]. The low energy particles are more dangerous than high energy particles for satellites as will be seen later in this chapter.

Charged particles are trapped in the Earth's magnetic field which are named as Van Allen Belts (or radiation belts). Van Allen Belts were discovered by Van Allen in 1958. Magnetosphere provides protection from cosmic rays and solar particles. The trapped particles gyrate helically around the magnetic field lines and the motion of the particles is constrained by the magnetic field.

As seen in Figure 2.7, there are two types of motion for trapped particles between north and south poles. One of them is a sliding motion or gyro motion along to the magnetic field lines. As the magnetic field is strong and as the particle penetrates this region, the gyro motion slows down. While particles penetrate the region where the magnetic field is strong, they would lose energy before entering the atmosphere. This results in the phenomena called northern and southern lights. The region where the particles reverse is called mirror point. Electrons and ions can remain trapped for a long time. This motion is known as bounce motion. Drift motion is described as perpendicular to the magnetic field lines. The trapped electrons and protons drift all

---

[1] Geomagnetic latitude is represented by λ in Figure 2.5. $|\theta_M|$ was used instead of λ for AMS-01 analysis.
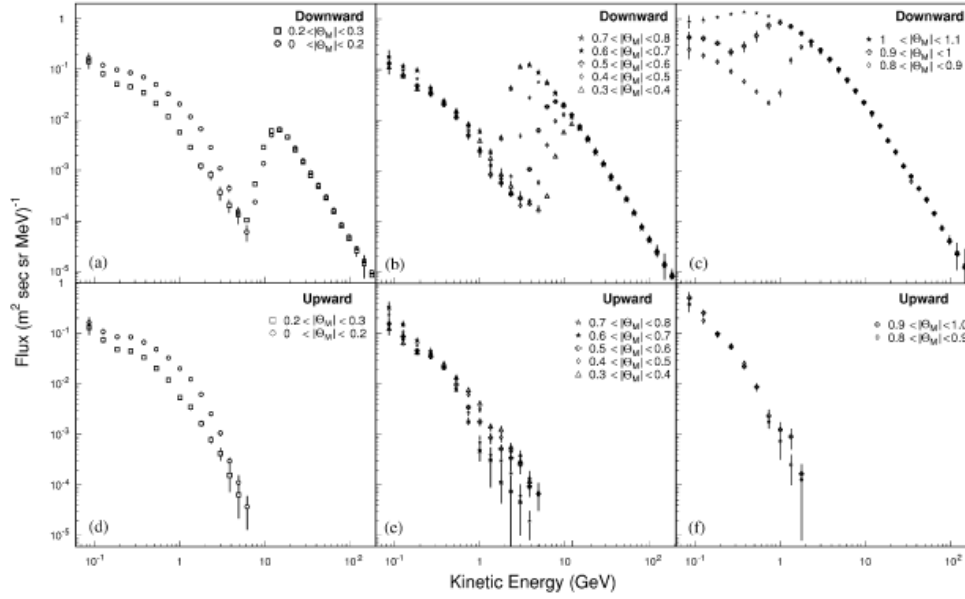
Figure 2.6: Flux spectra for (a-c) downward and (d-r) upward going protons [20]. The geomagnetic cutoff decreases with increasing geomagnetic latitudes, $|\theta_M|$ at Earth orbit. The trapped proton spectrum below the cutoff is observed to be similar for down going and up going particles.

the way around the Earth. Being positively charged, ions drift clockwise as viewed from north and electrons drift the other way. Earth's magnetic field allows only the most energetic and fastest particles to penetrate deep into the atmosphere [32].

Radiation belts consist of two distinct features, as shown in Figure 2.7, with the combination of protons and electrons in the inner belt which is centered at 10^4 km from the Earth's magnetic axis and outer belt consists of energetic electrons which are centered at 2.2×10^4 km from the Earth's magnetic axis with energies up 10 MeV [10]. These electrons and protons usually originate from solar activity.

Radiation belts vary with latitude. For example, below 1000 km altitude, intensity of trapped particles is related to magnetic field intensity, which decreases at low altitudes. There is a peak in the region where the magnetic field is lower. This region is located near the coast of Brazil and its name is South Atlantic Anomaly(SAA). Proton flux is intense in this region, therefore the region is a threat for electronic components of spacecraft which travel in low Earth orbit.

14
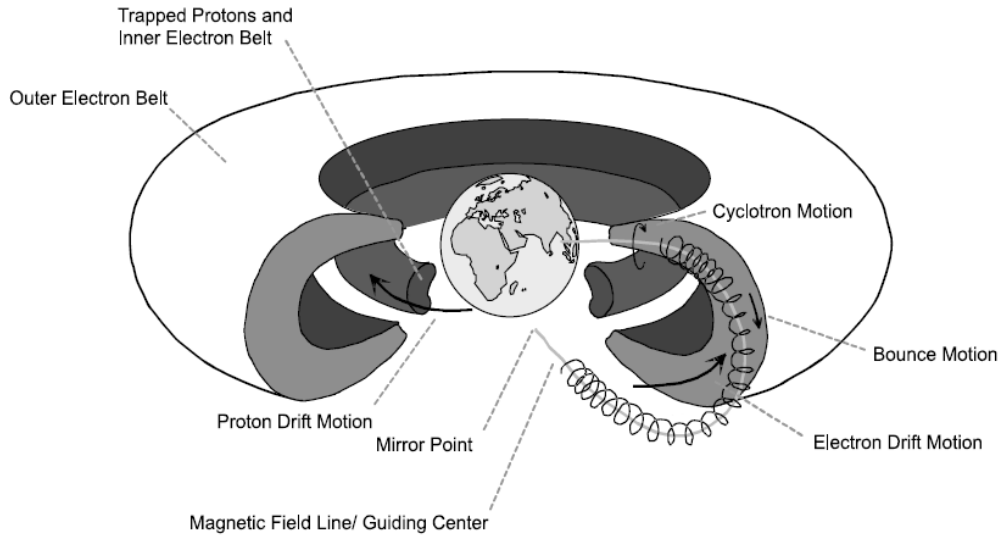
Figure 2.7: Trapped Protons and Inner Electron Belt and Outer Electron Belt. Proton drift motion is perpendicular to the magnetic field lines. Bounce motion is shown for trapped electrons and protons [13].

2.2.2   Galactic Cosmic Rays

Over all energies, cosmic rays consist approximately of 87% protons, 11% helium, 1% heavy particles, all of which are elements in the Periodic Table [24]. Figure 2.8 shows the constituents of cosmic rays. Galactic Cosmic Rays(GCR) are high energy charged particles that originate outside the Solar system. Origin of galactic cosmic rays is still a mystery, but it is thought that supernova explosions are the main source. Their energies can be up to 10^{11} GeV.

Galactic cosmic rays mainly cause Single Event Effects in microelectronics. Energy deposition is measured by their Linear Energy Transfer (LET) rate which is the energy deposited by the ionizing particle per unit path length in the sensitive volume [5].

2.2.3   Solar Events

The Sun flips its North and South magnetic poles every 11 years. The origin of this magnetic pole cycle is not yet well understood. There are two types of solar particles events named solar minimum and solar maximum, which depend on the number of

15
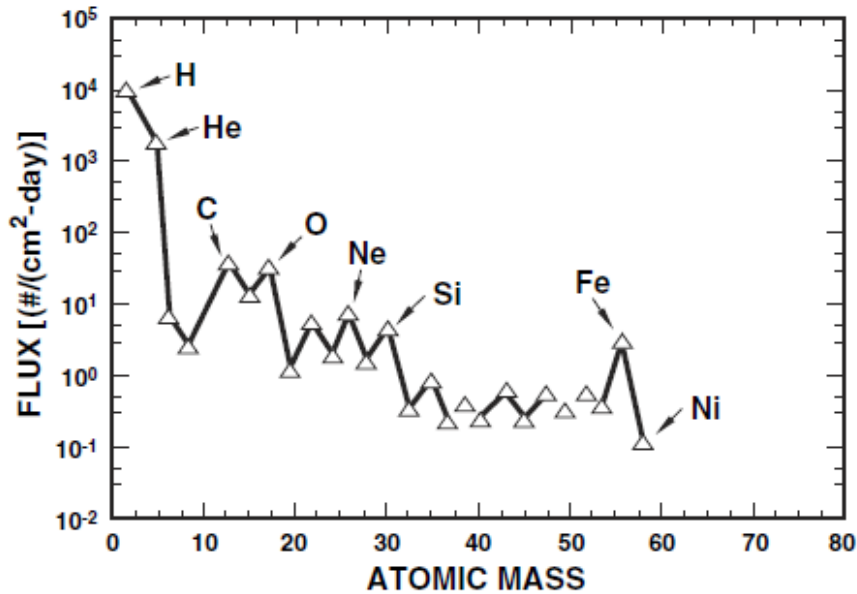
Figure 2.8: Relative abundance of elements in galactic cosmic rays. The flux of galactic cosmic rays changes with atomic mass [19].

active regions of the Sun known as sun spots. At a solar minimum, there are fewer sunspots or solar flares, and it takes approximately 4 years for a solar minimum to end. When solar minimum occurs, sometimes no sun spot is observed for many days. Figure 2.9 shows sunspot observations in the past 74 years and also expected sunspots numbers for future. Low energy protons and alpha particles are emitted mostly from these solar flares.

The particles coming from solar events have to be taken into consideration for space-craft. Some solar flare particles are trapped in the radiation belts which cause changes in particle intensities. Solar wind is associated with solar flares which cause eruption in the magnetic field towards the Earth and this also effects the galactic ray flux observed on the Earth. And therefore, devices are exposed to more radiation from solar winds in low earth orbit [19].

2.3   Interaction with Matter

A charged particle loses some amount of energy through single collisions while it is passing through matter. When the charged particle penetrates matter, it interacts

16
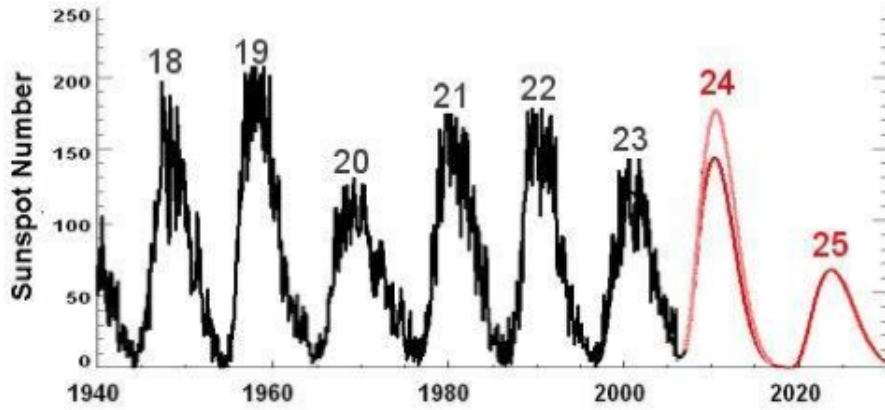
Figure 2.9: Sunspot numbers for approximately past 70 years and expected sunspot number for future [1].

with electrons and rarely with nuclei. The effects of the collision changes with the properties of the target material and with the energy and the type of the incoming particle. Furthermore, it depends on the thickness of the material and the number of the target particles per unit volume. All processes cause energy transfers from the incoming particle to the target material. Cross section is the probability of interaction. The total cross section can be defined as :

$$\sigma_{tot} = \int \frac{d\sigma}{d\omega} d\omega \tag{2.7}$$

$d\sigma d\omega$ is differential cross section, and $d\omega = \sin\theta d\theta d\phi$. Particles can interact in different ways. Equation 2.7 shows the measure of all interaction probabilities.

2.3.1 Bethe Bloch Formula

The mean rate of energy loss for charged particles in matter due to interactions is given by Bethe-Bloch equation as seen in Equation 2.8 [25]. Bethe-Bloch formula is valid only when the velocity of the particle is larger than the velocity of electrons in the atom of the target material. The energy loss is expressed in units $MeV cm^2/g$.

17

$$-\frac{dE}{dx} = 2\pi N_a r_e{}^2 m_e c^2 \rho \frac{Z}{A}\frac{z^2}{\beta^2}\ln\Big(\frac{2m_e\gamma^2 v^2 W_{max}}{I^2}\Big) - 2\beta^2 \qquad (2.8)$$

Two corrections, namely density effect correction and shell correction, have to be added to compare experimental results at a certain range as seen in Equation 2.9

$$-\frac{dE}{dx} = 2\pi N_a r_e{}^2 m_e c^2 \rho \frac{Z}{A}\frac{z^2}{\beta^2}\ln\Big(\frac{2m_e\gamma^2 v^2 W_{max}}{I^2}\Big) - 2\beta^2 - \delta - 2\frac{C}{Z} \qquad (2.9)$$

Density effect is only appreciable for particles with high kinetic energy. It may be ignored at low kinetic energies. As the velocity of the particle increases, collisions cause a larger energy loss. Density correction also depends on the density of the target material [25]. Shell correction is important only when the velocity of the incident particle is smaller than the velocity of electrons in the target material [27]. In addition to the shell and the density corrections, Bethe-Bloch formula can be modified by ultra relativistic velocities, high order QED processes and high order terms related to cross section. However, for the primary particles, Bethe-Bloch formula with the shell and the density corrections is more suitable [25].

$2\pi N_a \mathrm{r}_e^2 \mathrm{m}_e c^2 = 0.1535$ MeVcm$^2/g$

r_e: electron radius (2.817×10^{-13}) cm

m_e: electron mass

N_a: Avogadro's number

A: Atomic weight of target material

Z: Atomic number of target material

$\beta = v/c$ of incident particle

z: charge of incident particle

ρ= density of target material

$\gamma = 1/\sqrt{1-\beta^2}$

δ: density correction

C: shell correction

I: mean ionization potential

W_{max}: maximum energy transfer for only collision
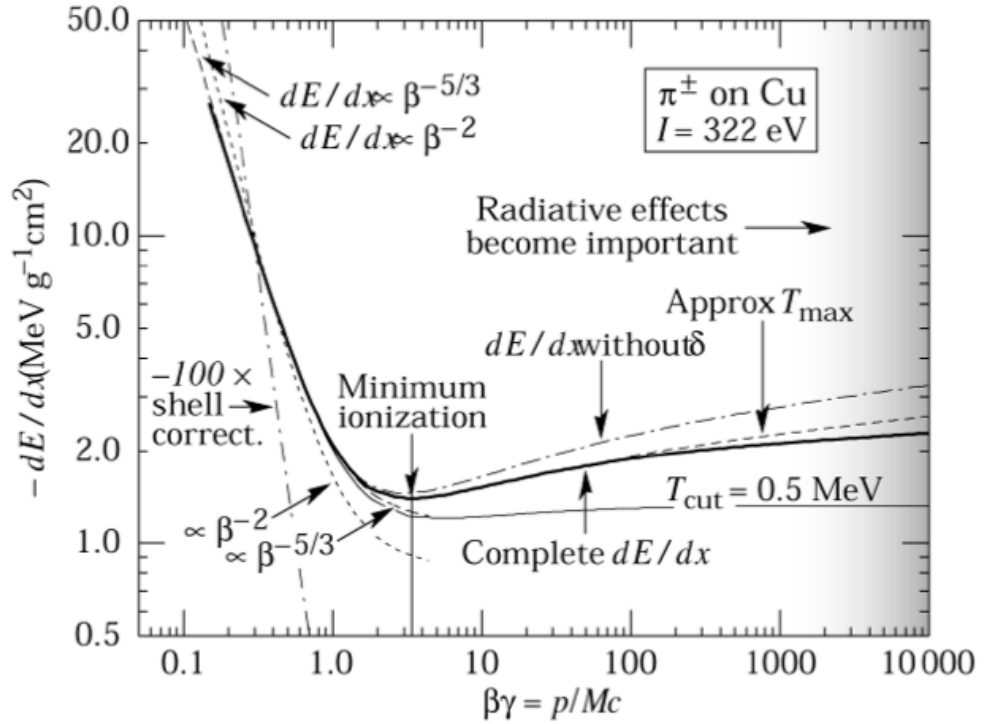
Figure 2.10: Energy loss for pions in copper [3].

Figure 2.10 shows energy loss for pions in copper according to the Bethe-Bloch equation. Due to $\frac{1}{\beta^2}$, which is a kinematic factor, the energy loss decreases sharply for low velocities. As can be seen in the figure, when $(\beta\gamma)$ value is around to 3-4 or $\beta = 0.96$, which is independent from the target material, the minimum ionization can be observed. The particles which lose their energy near the minimum ionization are named Minimum Ionizing Particles. If the particle has higher energy due to their large energy transfer, energy loss increases slightly.

As can be seen in the figure (dE/dx without δ with dash-dotted curve), saturation at large energy occurs due to the density effect. The complete energy loss with adding all corrections is shown as bold line curve [3].

2.3.1.1 Bragg Curve

While particles pass through some material, they lose all their kinetic energy eventually. The range of the particle traveling in the material changes with the kinetic energy of the particles. As the particles traverse the material, the energy loss increases near

19

the end of the trajectory. The maximum energy loss abruptly happening at the end of the particle trajectory is named as the Bragg Peak. This energy transfer can lead to damage in the structure of material or molecule bonds. This is the main reason for serious damage to electronic components of satellites when they are exposed to radiation.
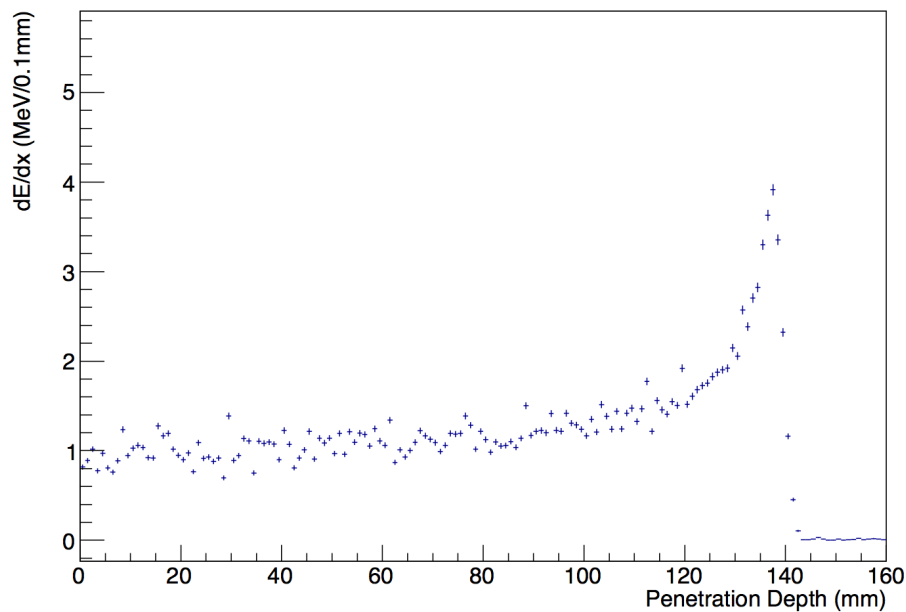
Figure 2.11: For Si target 200 MeV protons energy loss of per unit length. Generated using Geant 4.

For example, Figure 2.11 shows how stopping power changes with path length while the particle penetrates into the material using a GEANT4 simulation. As seen in the figure, 200 MeV protons penetrate 14 cm Si target.

Although, energy loss mechanism of charged particles cause damage for the electronic components, they are also used for one of the different kinds of cancer treatment, namely hadron therapy. Chemotherapy or radiation therapy techniques are applied to parts of the patients' body which do not have infected cells. Hadron therapy thanks to the Bragg curve, can be applied to the desired depth of the tumor accord-

ing to different types of cancer [36]. Figure 2.12 shows a Bragg peak for different proton energies generated with GEANT4 for tissue material. The penetration depth increases as particle energy increases; for this reason Bragg peak decreases. As seen in the figure, particle energies can be arranged for different tumor depths.
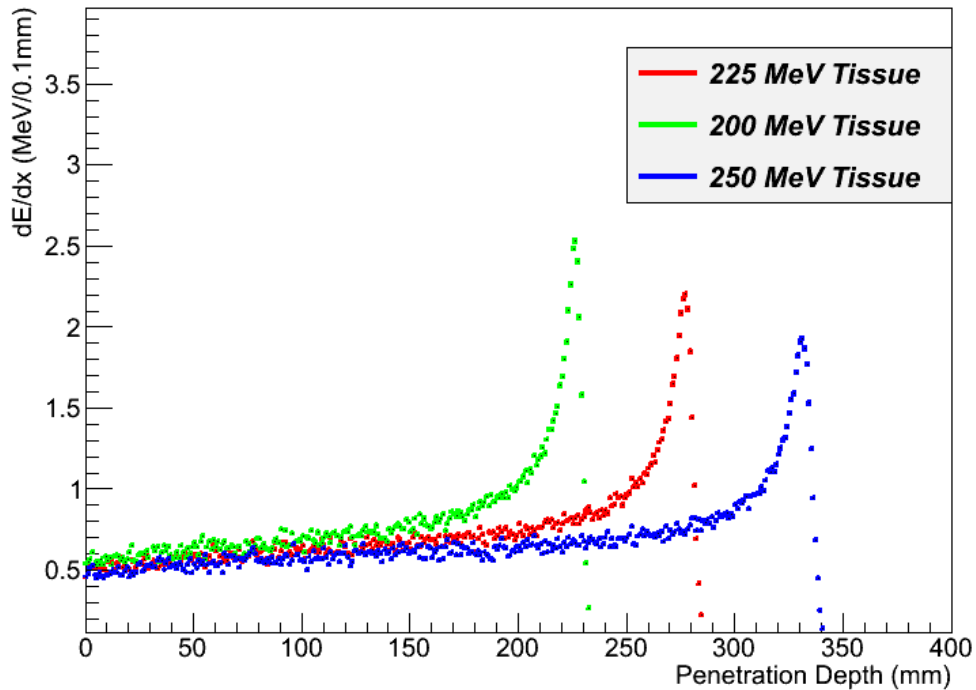
Figure 2.12: Bragg peak for different proton energies generated with GEANT4 for tissue material. Maximum energy loss depends on the particle energy. Thus, different particle energies can be used for hadron therapy for different tumor depth.

2.4 Space Radiation Effects

Space radiation environment can be dangerous for electronic components which are used for space applications. These electronic components have to be checked whether they can resist to space radiation or not, before launch. Space radiation effects can be classified into three categories: Single Event Effects (SEEs), Total Ionizing Dose (TID) effect and Non-Ionizing Dose Displacement Damage Effects.

These effects are a big challenge for reliability and performance of the electronic

components. For this reason, it is important to understand how charged particles interact with electronic components which problems might occur and how to solve them.

2.4.1 Single Event Effects

The interaction of primary or secondary ionizing particles with electronic components produces electron-hole pairs in electronic components. Production energy of these pairs depends on the target material. For example, a minimum energy of 3.6 eV for silicon, 4.8 eV for GaAs and 2.8 eV for germanium are required create electron-hole pairs. If the energy of produced electron-hole pairs is higher than the minimum energy, additional electron-hole pairs can be produced [19].

These pairs are generated as direct ionization or indirect ionization as particles lose energy. Direct ionization is the generation of electron-hole pairs by the primary particle. Any heavy ion with atomic number greater than two can produce the necessary number of pairs to cause upsets in devices.

Indirect ionization is defined as interaction of light particles with the nuclei through nuclear interaction. Lighter particles such as protons do not cause enough electron-hole pairs by direct ionization. When protons or neutrons strike the device, first nuclear reactions occur and then the produce of these reactions cause generation of electron-hole pairs along their path. These nuclear interactions can result in the emission of gamma or alpha particles or the spallation of the target nuclei. They in return create the number of required pairs to cause single event effects.

$$LET = (1/\rho)\frac{dE}{dx} \tag{2.10}$$

Linear Energy Transfer(LET) is described as a measure of deposited energy per unit length due to ionization when the energetic particle passes through the material. Unit of LET is $MeV \cdot cm^2/g$. It is related to the particles' charge deposition. Stopping power is not equal to LET, but it approximates Linear Energy Transfer (LET) as seen in Equation 2.10. LET values can be calculated for target material, for instance LET

22

value of silicon is 97 $MeV \cdot cm^2/g$ with $1pC/\mu m$ charge deposition. If the density of the target material ρ, is multiplied by the LET value, this gives the energy loss in units of MeV/cm. Integration of this equation gives the total deposited energy.

As mention above, while the particles travel through the material, electron-hole pairs are created. Minimum LET value required to create pairs which cause single event effects are named critical LET or LET threshold. LET value vary with the particle's energy and mass, and type of the material [2].

Trapped particles in the Van Allen radiation belts are the main source of SEEs. Especially, these errors are the main threat for satellites in LEO. Exposure to radiation affects the functionality and performance of electronic components of satellites as days go on. For this reason, radiation assurance tests are important for the reliability of electronic components.

SEEs can be classified as hard errors which are non-recoverable and soft errors which are recoverable errors. Soft errors can be removed by resetting or reinitializing the system. On the other hand, these errors might cause loss of data. Single Event Upsets(SEUs) is a soft error example. Hard errors effect the performance of electronic components and damage the component permanently, for example Single Event Latch-up (SEL) and Single Event Burnout(SEB).

2.4.1.1 Single Event Upsets(SEUs)

Single Event Upsets (SEUs) are defined as radiation induced errors and these errors occur when the primary or secondary particle hits a sensitive part of the electronic component. SEUs are classified as non-destructive effects or soft errors which cause damage to registers and digital devices [38].

SEUs usually cause bit flips in memory cards and registers. It leads to a change in a bit from logical 0 to logical 1 or logical 1 to logical 0. Figure 2.15 shows SEUs in a shift register. Signals shown in top are SEU indicators and signals below are outputs of the shift register. Figure 2.13(a) shows the expected normal signal of the register. Figure 2.13(b) exemplifies a dynamic SEU which leads to a change in the logic state of the bit during the operational time. As seen Figure 2.13(c) shift register

is connected to another part of register. Figure 2.13(d) is an example of a static SEU which leads to a change in configuration bits. Here, the register was broken off and input was connected to 0 [2].
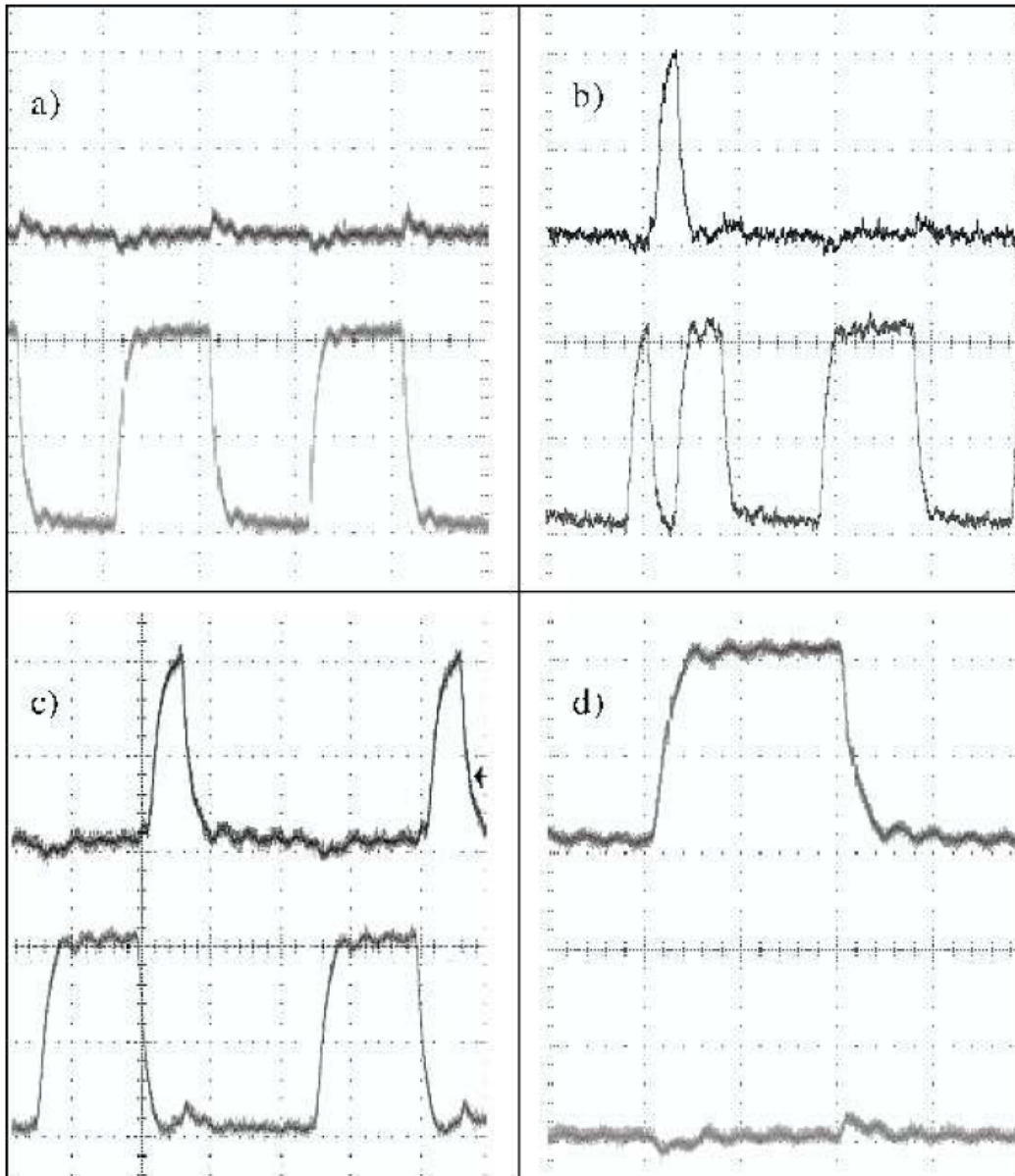

Figure 2.13: Dynamic and static SEUs example. Upper signals are SEU indicators, and bottom signals are output. (a) shows operational signals, (b) shows dynamic SEU signal example, (c) shift register connected to other part of register, (d) input of shift register shows 0 [9].

Generally, galactic cosmic rays, solar particles, especially solar flare particles and

trapped particles in radiation belts cause SEUs. Protons are the main source of errors in LEO and they cause SEUs by complicated nuclear interactions. SEUs are also encountered by satellites in the South Atlantic Anomaly. These errors must be taken into account not to cause unexpected failures.

2.4.1.2   Single Event Latchup(SEL)

The most known hard error is Single Event Latchup (SEL). It is a destructive error and it occurs due to triggered energetic protons, neutrons and heavy ions. These particles cause short circuits in the device. The device cannot go back to its original state when this error occurs.

2.4.1.3   Single Event Burnout(SEB)

Single Event Burnout (SEB) occurs when heavy ions pass through the target material. This error happens only with power devices like MOSFET (metal oxide semiconductor field effect transistors) at high voltages. This event is also an example of a hard error.

Single event latchup and single event burnout radiation tests are carried out using heavy ion sources. TAEK PAF is a source of protons and cannot be used for single event latchup and single event burnout error tests.

2.4.2   Non-Ionizing Dose Displacement Damage Effects

Energetic particles also cause non-ionizing effects on electronic components. Non-ionizing dose displacement effects occur due to energy transfer while an incident particle passes through the material. The particle dissipates energy by exciting orbital electrons and by elastic collisions with the material nuclei. In general, protons cause this effect. Displacement damage can be quantified using the non-ionizing energy loss (NIEL). The NIEL is energy lost to non-ionizing events per unit length, MeV/cm or MeV$\cdot$cm^2/g.

2.4.3 Total Ionizing Dose

Total Ionizing Dose (TID) is a permanent error when the component is exposed to radiation continuously. Protons, heavy ions and alpha particles all contribute to this effect by changing the electronic properties of the device. The amount of ionization depends on the deposited energy per unit mass of target material and it is expressed as radiation absorbed dose. The radiation absorbed dose unit is given by rad or $Gray$.

$$1Gray = 1J/kg = 100Rad \tag{2.11}$$

Equation 2.11 shows relationship between rad and Gray. Gray is an amount of absorption per kilogram of matter.

TID radiation tests can be carried out with using Cobalt-60 or other sources. A 300000 Cu Co-60 source in TAEK SANAEM Facility can be used for carrying out TID radiation tests according to ESA and NASA Standards. It is important to gain certification of electronic components and to give service in national or international space application area. SEEs radiation tests have not been carried out in Turkey yet. This requirement would be satisfied when the laboratory and construction as suggested by this thesis is completed.

CHAPTER 3

DESIGN OF AN IRRADIATION FACILITY FOR SEE TESTS

3.1 Introduction

Single Event Effect radiation tests are carried out using different energy ranges of proton and heavy ion sources. While energy of heavy ion sources range from 1 MeV/u to 1000 MeV/u, proton sources range from 20 MeV to 500 MeV as seen in Table 3.1 [19]. The table shows the most used facilities for SEE tests all over the world. These radiation test facilities are used according to type of device, type of error and type of environment being studied.

Figure 3.1 was plotted for a satellite which is similar to Göktürk-2 at 800 km heliosynchronous orbit. A satellite with 1 mm silicon shielding was exposed to trapped protons randomly for a year duration by using SPENVIS [12]. The information of trapped protons was taken and the output used for GEANT4 which simulates particles passing through matter [7]. Carbon shielding of 2 cm thickness was exposed to these trapped protons. According to the figure, particles with energies less than 20 MeV stop in the shielding. On the other hand, higher energy particles pass through the shielding, losing energy and becoming less energetic. Because of this fact, particles having energies higher than 20 MeV, have to be taken into consideration for the tests of electronic components. This figure also explains why PAF's energy value is suitablefor SEE radiation tests.

Table 3.1: Single Event Effects Test Facility Properties

| Facility Name	Type of Source	Energy Range
Brookhaven National Laboratory SEU Test Facility Upton, NY	Heavy Ion	1-10 MeV/u
Texas A&M University Cyclotron Institute College Station,TX	Heavy Ion	1-40 MeV/u
Lawrence Berkeley National Laboratory 88-inch Cyclotron Berkeley, CA	Heavy Ion	4.5-16 MeV/u
Brookhevan National Laboratory NASA Space Radiation Laboratory Upton, NY	Heavy Ion	80/170 MeV/u
Indiana University Cyclotron Facility Bloomington, IN	Proton	35-200 MeV
TRIUMF Proton Irradiation Facility Vancouver, BC, Canada	Proton	20-500 MeV
University of California at Davis Crocker Nuclear Laboratory Davis, CA	Proton	1-63 MeV
Francis H. Burr Proton Therapy Center Boston, MA	Proton	15-230 MeV
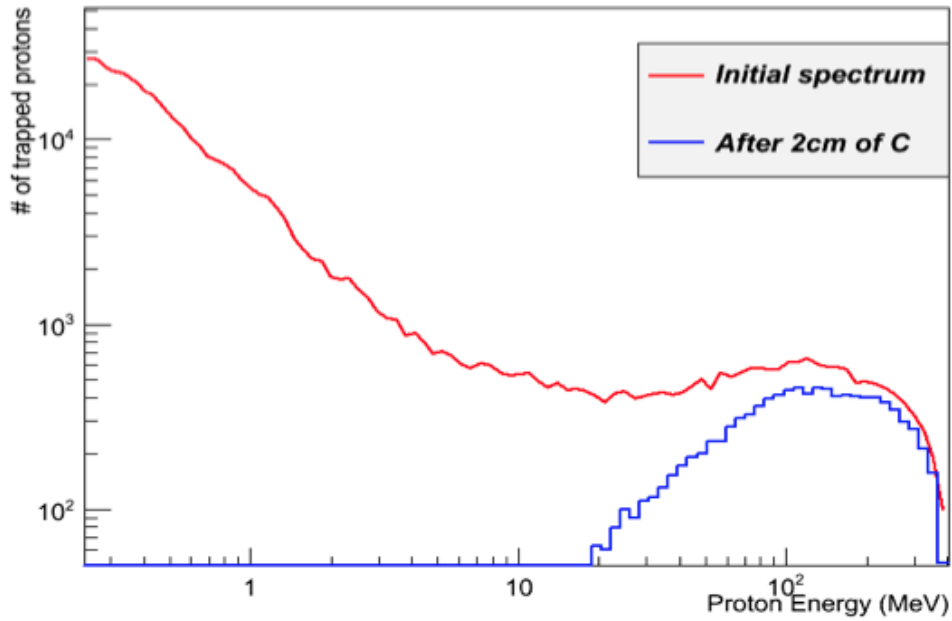
Figure 3.1: GEANT4 Simulation for trapped protons at 800km and heliosynchronous orbit. After the target, particles with energies higher than 20 MeV pass through the material. These particles can damage electronic components of satellite. Generated by using GEANT4.

3.2 TAEK SANAEM Proton Accelerator Facility

Proton Acceleration Facility(PAF) was inaugurated on 10th of May 2012 and has been commissioned by TAEK, founded in Ankara in 1956. PAF has four arms and three of these arms are used for radioisotope production, and two of them can be used as simultaneous output beams. The produced isotopes are ^{11}C,^{15}O useful for positron emission tomography and ^{18}F for single photon emission computed tomography and ^{111}In,^{67}Ga and ^{123}I for gamma cameras [34]. The other arm is reserved for R&D research.

According to Table 3.2, the minimum current of PAF is 12 μA, while the minimum beam size is 1 cm and minimum beam flux is 2.05×10^{11} p/s/cm^2. When PAF delivers 12 μA current which corresponds to a flux of 2.05×10^{11} p/s/cm^2, these values are too high for irradiation applications. In order for ESA Standards on SEE radiation tests to be applied, beam flux should be at least 10^8 p/s/cm^2. Large beam size is also

Table 3.2: TAEK PAF Accelerator properties

Accelerator Type	Circular-Cyclotron
Accelerating beam type	proton
Total number of beam lines	4
Number of simultaneous output beam	2
Proton beam energy	15-30 MeV variable
Proton beam current	12 μA-1.2mA
Magnetic field	0.12-1.7 Tesla

desirable for irradiation applications without extra target damage.

According to ESA/SCC 25100 standard:

- Radiation source should be a particle accelerator and LET values of protons or heavy ions should be used for these tests.

- The energy range of the particle accelerator can vary for protons from 20 MeV to 300 MeV.

- Particle flux should range from $10^5 \ p/s/cm^2$ to at most $10^8 \ p/s/cm^2$.

- The temperature of the components should be recorded while it is still being tested.

- Test should last at most 20 minutes for each component. All values and steps should be indicated in the test report.

- Within the standard, single event upset, single event latch-up or single event burnout tests can be done.

Using GEANT4, various beam line parameters have been studied to examine behavior of particles for different cases. For example, Figure 3.2 represents energy loss per unit

length for 30 MeV protons which hit the silicon target after moving 10 cm in vacuum. As can be seen in the figure, 30 MeV protons lose all kinetic energy after about 5 mm in silicon. As the electronic components thickness are often only a few micrometers, 30 MeV protons are suitable for SEE tests.
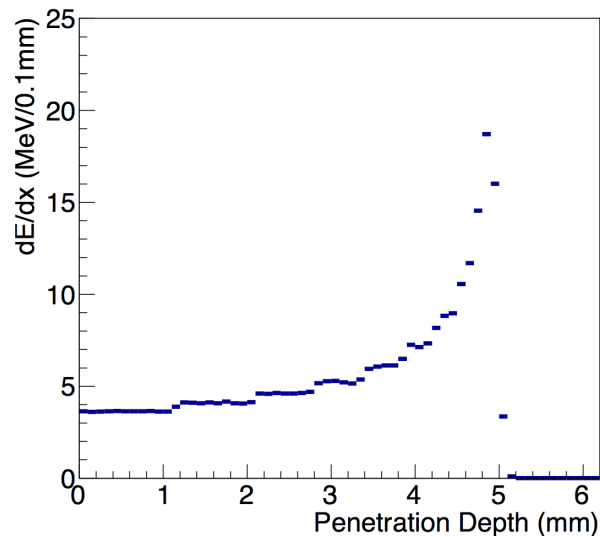

Figure 3.2: For 30 MeV protons energy loss per unit length, protons penetrate 5 mm in silicon target. Generated by using GEANT4 [15].
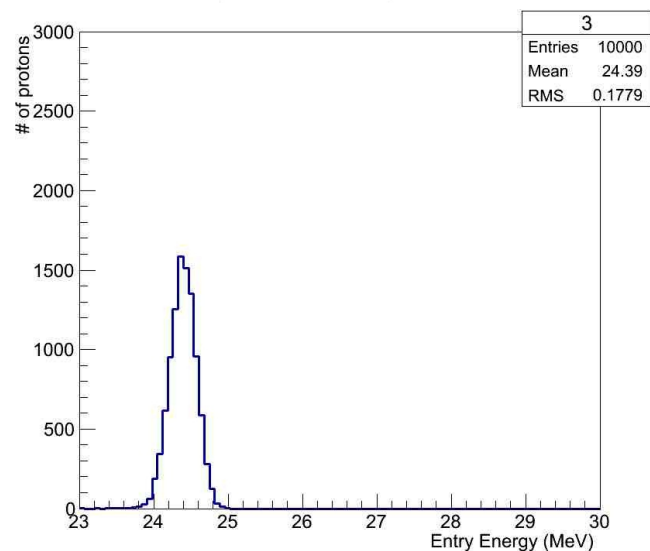

Figure 3.3: Beam energy after 3 m in air. Generated by using GEANT4.

One of the first design considerations is whether the beam will travel in vacuum or in air. This was studied initially using a GEANT4 simulation. Figure 3.3 shows the

beam energy after traveling 3 m in air. The beam energy is approximately 24 MeV after traveling in air and decision was made to design the beamline with vacuum due to a large quantity of beam energy loss in air.
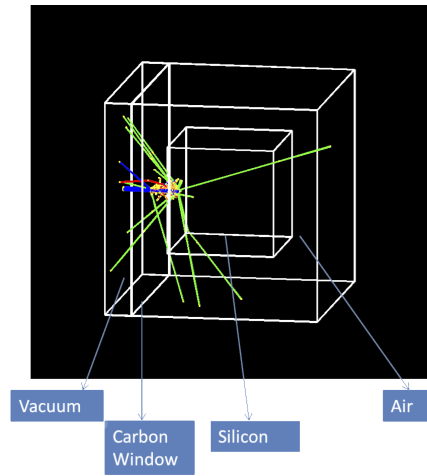

Figure 3.4: Protons travel 5 cm in vacuum, pass through a carbon window, and travel 5 cm air before hitting the target [15].

Figure 3.4 shows 30 MeV protons traveling 5 cm in vacuum and passing through a carbon window before hitting a silicon target. The blue line is represent primary (positive) particles and the red and green ones are secondary particles (respectively negative and neutral). A window is placed before the silicon target. This GEANT4 simulation was performed to study different window materials and a suitable window thickness. Figure 3.5, Figure 3.6 and Figure 3.7 show how the energy of beam changes with carbon, aluminum and mylar windows in thicknesses of 0.5 mm, 1 mm and 2 mm. Figure 3.8 shows the energy of beam after carbon, aluminum and mylar windows thickness of 1 mm. As can be seen from the figures, a mylar window minimizes energy loss value.

In order to get proper flux value and the necessery large target irradiation area, the beam size should be extended using dipole and quadrupole magnets. A dipole magnet bends the beam to guide the particles to target while a quadrupole magnet focuses particles in one plane and defocus them in the other-plane. The beam line has four quadrupole magnets and one 5 port switching magnet from the cyclotron. One dipole magnet and two quadrupole magnets are planned to be employed in order to produce a defocused beam at the target area.
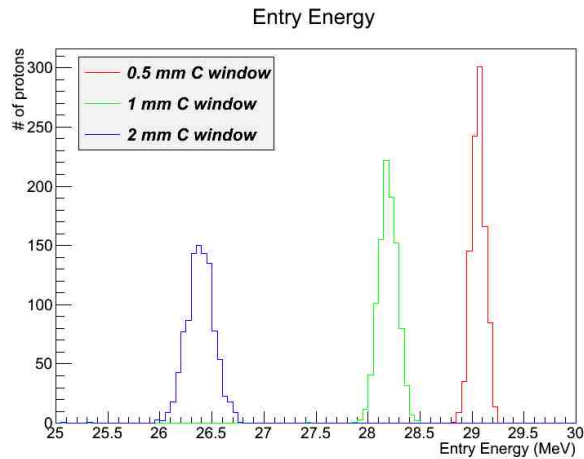
Figure 3.5: Energy value of beam particles after hitting carbon window with different thickness.
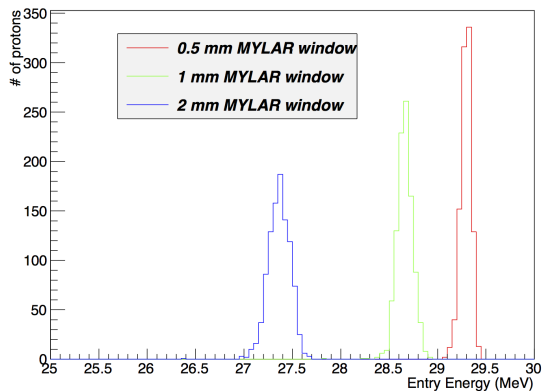

Figure 3.6: Energy value of beam particles after hitting mylar window with different thickness.

Figure 3.9 and Figure 3.10 show a primary design presented at 9th International Conference on Radiation Effects on Semiconductor Materials Detectors and Devices, in Florence, Italy in 2012. The figures show respectively horizontal and vertical beam line views after two quadrupole magnets. The quadrupole magnets are shown in orange. Location of beam particles can be defined along two axes, x and y at any point. If the beam line has no collimator or if there is nothing to reduce the number of beam particles, all particles can be simulated according to x, x', y and y' values of their locations using MADX [18]. x' and y' are the divergence of the beam along z. The
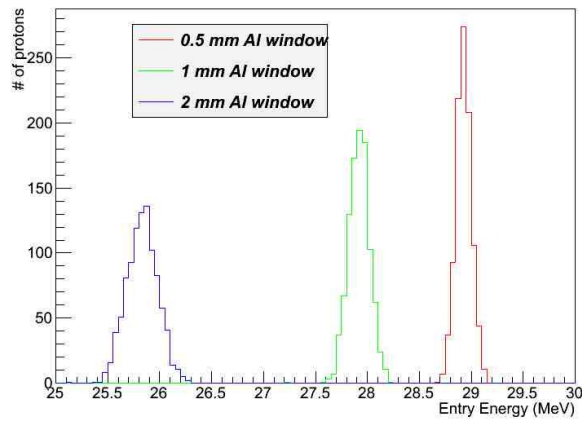
33

Figure 3.7: Energy value of beam particles after hitting aluminum window with different thickness.
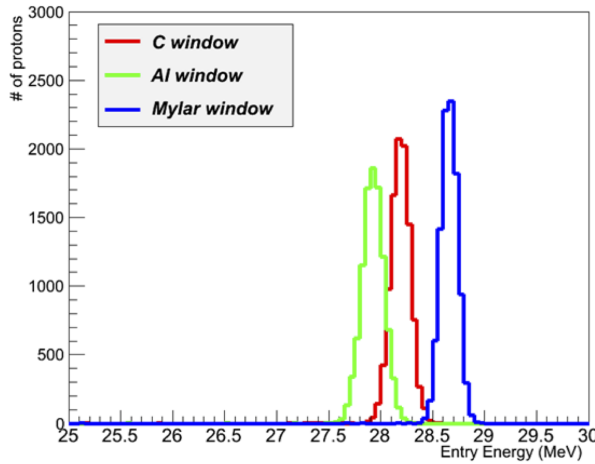
Figure 3.8: Energy value of beam particles after hitting carbon, aluminum and mylar window. Mylar with 1 mm thickness is suitable, providing less energy loss.

x-x' and y-y' plots remain in the shape of an ellipse in the simulation. The shape of ellipse can change, but the area of the ellipse remains the same. In this simulation, the initial beam size is 1 cm and the final size is 10 cm after the magnets.

In the next iteration 2 dipole magnets and 6 quadrupole magnets, 2 Cu foils and a collimator were added with the goal of a 20 cm final beam size in FLUKA design.

Figure 3.11 shows this design using two dipole and six quadrupole magnets. The first and the sixth small squares are dipole magnets while the others are quadrupole

34

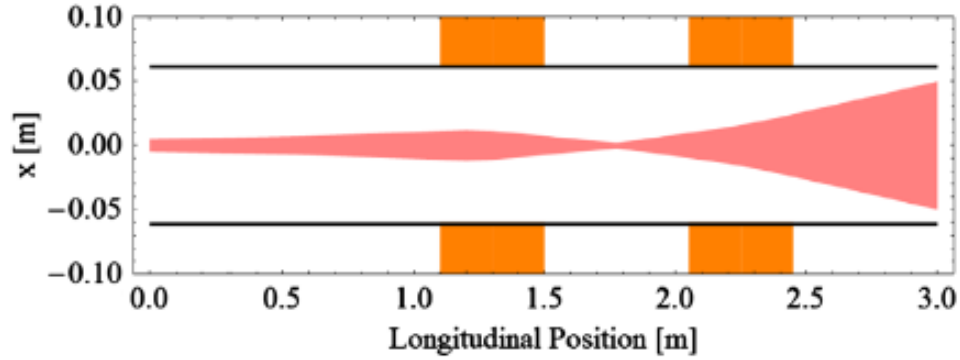Figure 3.9: Horizontal beam line optics after two quadrupole magnets. The beam line size reaches 10 cm after traveling 3 m. Generated by using MADX [15].

Figure 3.10: Vertical beam line optics after two quadrupole magnets. The beam line size becomes 10 cm after traveling 3 m. Generated by using MADX [15].

magnets. The design was studied from the cyclotron onwards and the final beam diameter is 10 cm. This study belongs to Ayşenur Gencer and the graph was examined using the MADX beam optics program [8].

Figure 3.12 shows cyclotron and R&D room at TAEK SANAEM. As can be seen the figure, the beam line has four quadrupole magnets and a 5 port switching magnet. TAEK wants to use the 5 port switching magnet for other R&D projects.

Reduction of flux with collimators and foils is employed using a FLUKA simulation [14]. The MADX beam optics was combined with the FLUKA design. This thesis contains foil and collimator design simulations for reducing the flux using FLUKA and its results will be presented in the next sections.
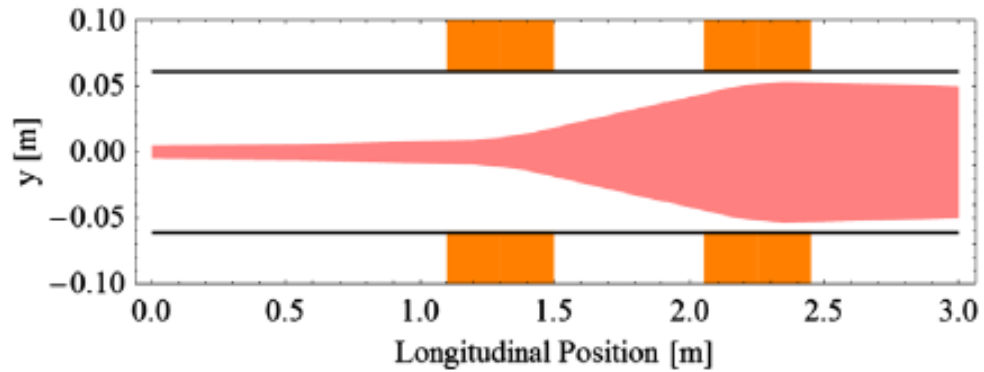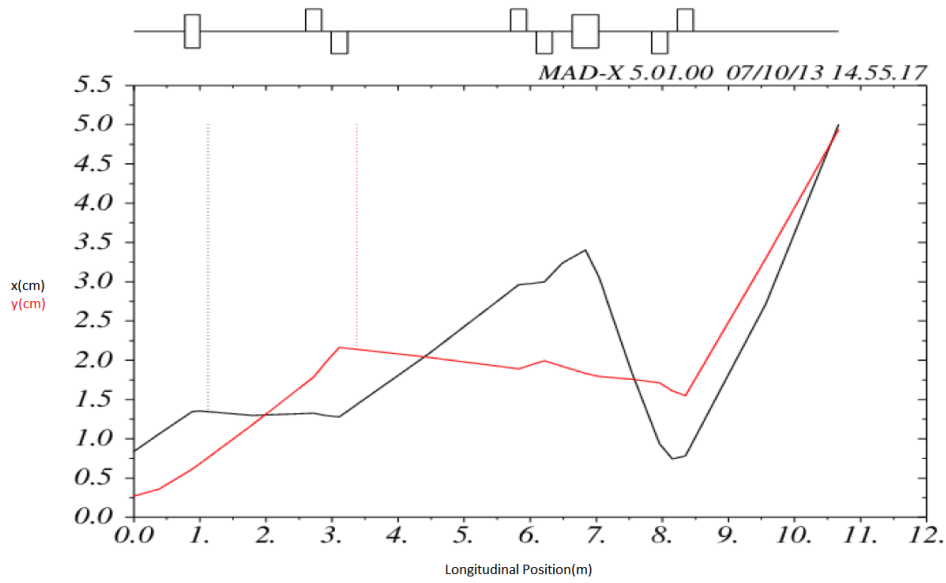
Figure 3.11: The beam line view after two dipole and six quadrupole magnets. The beam line size becomes 10 cm after traveling 3 m. Generated by using MADX [15].
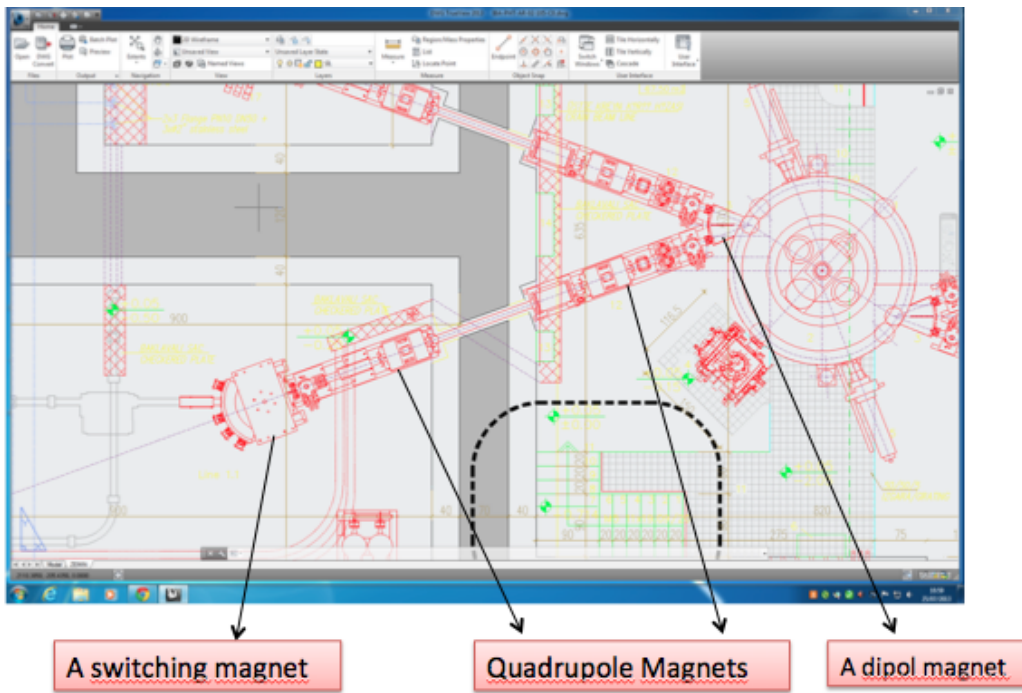

Figure 3.12: Drawing of TAEK SANAEM PAF includes the cyclotron and R&D room.

36

3.2.1 Reducing the Fluence by Using Foils

FLUKA is a Monte Carlo simulation package, developed by CERN, which is used for modeling particle transportation calculations, interactions with matter, electron and proton accelerator shielding design, dosimetry, cosmic ray and radiotherapy. FLUKA can simulate the interactions in matter of 60 different particles with energy range from keV to thousands of TeV with highest accuracy.

The first step is to reduce the number of particles using suitable foil thickness. Flux of the PAF has to be decreased by 1/2000 times to get the maximum flux value of the ESA Standard. It means that the number of particles must correspond to 5×10^{-4} proton/primary after the foils. In order to define suitable foil thickness, many simulations have been performed. The beam is placed at (0, 0, -10) cm and foils with different thickness are examined. Fluence is calculated as track length density by FLUKA US-RBIN detector in units of particles/cm^2 per primary. For this reason, dimensions of the detector is important in calculating the number of particles.

For 30 MeV protons, dE/dx value is 11 MeV/cm^2/g for Cu target [25] and they stop after 0.3 cm in Cu target. Foils can change the energy of beam particles by a small amount, thus they must be thin and resilient to irradiation. Foils with different thicknesses and detectors with different dimensions are studied to get the number of primary particles. Si detector is used with dimensions $20 \times 20 \times 1\ cm^3$ at 100 cm on the z-axis. If the Si detector is used to calculate the track length, a foil with 150 μm of thickness is suitable to reduce the flux value. According to Table 3.3, the number of particles has been decreased by 1/1000 times after only one foil.

Pencil beam, which is described to have zero dimensions, has been simulated to examine the number and the energy of particles. 5×10^5 primary beam particles travel in vacuum and hit Cu foils. First foil is placed at 0 on z-axis and distance between two foils is 0.5 cm. Figure 3.13 and 3.14 show the energy value of protons after the Cu foils. The number of primary and secondary particles and the energy of beam has been shown in Table 3.3 for this geometry. The values of energy are 0.29 GeV/cm^3/primary after the first foil and 0.26 GeV/cm^3/primary after the second foil. After the foils, proton energy is suitable for radiation tests according to the standard.
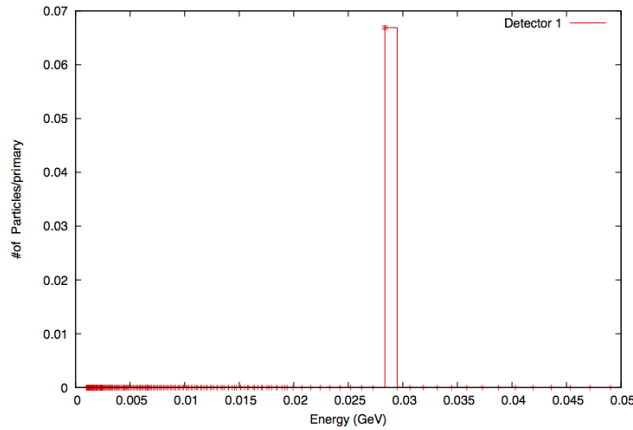
Figure 3.13: After one Cu foil energy of the beam particles is 0.29 GeV/cm^3/primary. Generated by using FLUKA.
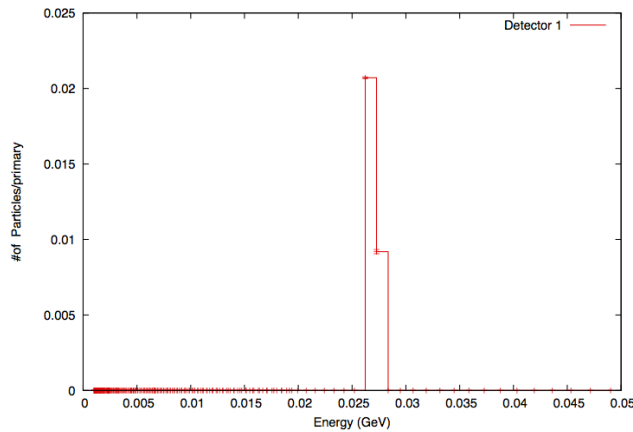
Figure 3.14: After two Cu foils energy of the beam particles 0.26 GeV/cm^3/primary. Generated by using FLUKA.

Figure 3.15 shows the fluence of particles in units of particles/cm^2·primary for the same geometry. This scattering angle can be simulated using USRYIELD detector in FLUKA. Figure 3.16 shows that the scattering angle has a peak value of 47 mrad. The beam is widened due to multiple scattering in the foil. Figure 3.15, the red widening line corresponds to the main irradiation area. Secondary particles, i.e neutrons, emerge due to multiple scattering after hitting foils. However, secondary particles are not desirable for radiation tests. For this reason, a collimator has to be used for stopping secondary particles. A collimator with 0.5 cm diameter is planned to be placed after hitting the foils. Not only does the collimator kill the secondary particles, but

Figure 3.15: After two Cu foils, simulation of beam particle fluence particles/cm^2 ·primary. Generated by using FLUKA.
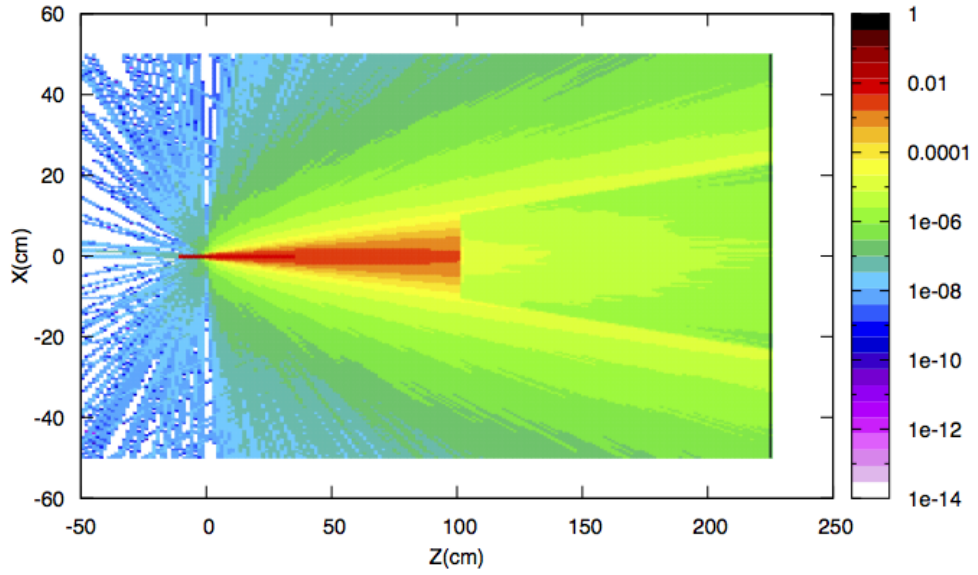
Table 3.3: Energy of Beam Particles and Number of Particles

Number of Foils	Number of Particles	Number of Neutrons	Protons Energy
1 Cu Foil	2.45×10^{-3} p/pr	5.37×10^{-8} neut/pr	0.29 GeV/cm^2/pr
2 Cu Foils	2.47×10^{-3} p/pr	2.47×10^{-8} neut/pr	0.26 GeV/cm^2/pr

also the number of particles decrease and the beam size gets smaller. The beam has a rectangular shape which has a width of 0.89 cm and 0.27 cm in this simulation. This beam width value belongs to PAF from the cyclotron.

Figure 3.19 shows the screenshot for foils and the collimator. The simulation consists of two Cu foils before the collimator and one Cu foil after the collimator.

After studying collimators with diameter 1 cm and 0.5 cm, the number of beam parti-cles and energy values are shown in Table 3.4. FLUKA requires a target to calculate the number of particles, for this reason a third foil is added after the collimator. As
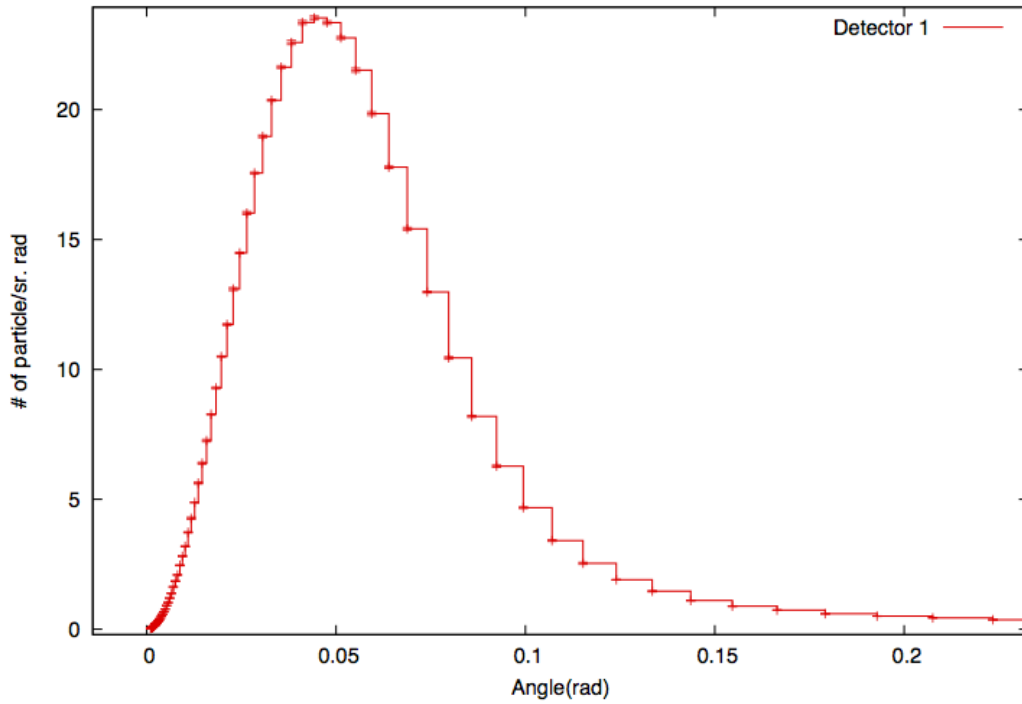
Figure 3.16: Simulation of beam particles scattering angle value is 47 mrad, after two foils. Generated by using FLUKA.

Table 3.4: Energy of Beam Particles and Number of Particles after hitting a collimator

Number of Foils	Number of Particles	Colimator diameter	Protons Energy
1 Cu foil	$3.9 \times 10^{-4} p/pr$	1 cm	0.25 GeV/cm^2/pr
1 Cu foil	$5.6 \times 10^{-4} p/pr$	0.5 cm	0.25 GeV/cm^2/pr

can be seen in the table, the collimator helps reduce the number of beam particles. According to the table, the number of beam particles are 5.6×10^{-4} p/pr with 10×10 cm^2 detector and 0.5 cm diameter of the collimator, and the required flux has been reached. The exact number can be refined by further studies.

The fluence values of all particles after the foils and the collimator can be seen in Figure 3.17. Figure 3.18 shows only the fluence values of the beam particles. Fluence of secondary particles is simulated by subtraction of two fluence values shown in Figure 3.20. A detector must be used in all FLUKA simulations to examine the behavior of particles. For this reason, secondary particles can also emerge from hitting
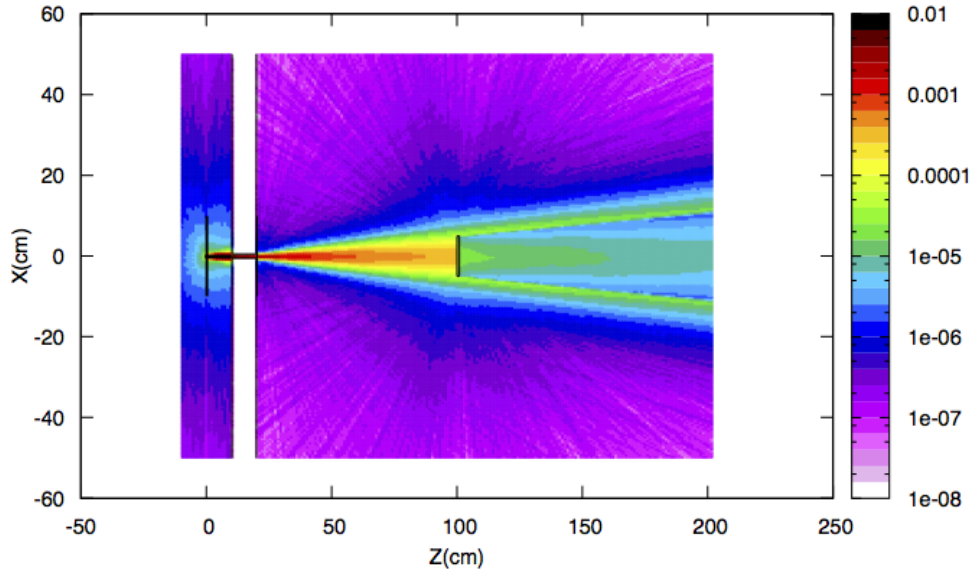
Figure 3.17: After the foils and collimator, fluence of all particles simulation in units particles/cm^2·primary. Generated by using FLUKA.

Si detector.

Temperature increase due to interaction of the beam with the target materials is a concern for the design.Temperature increase in a material can be calculated according to Equation 3.1. For 1 cm Cu target dE/dx=97 MeV/cm and for 0.015 cm Cu dE/dx= 1.47 MeV. Necessary cooling has to be provisioned in order not to damage the beam line and experimental area.

$$\Delta T = dE/dx \frac{N_p}{2\Pi \cdot \sigma_x \cdot \sigma_y \cdot \rho \cdot c_p} \tag{3.1}$$

N_p : number of particles 7.5×10^{13} p/sec.
c_p : heat capacity equals to 0.38 $J/g \cdot K$ for Cu
ρ: is the density of copper equals to 8.9 g/cm^3
σ_x, σ_y : beam width in units of cm, for PAF σ_x=0.2 cm σ_y=0.8 cm

Temperature increase in a foil with dimensions $10 \times 10 \times 0.015$cm^3 is equal to 5 K/p/s.

41
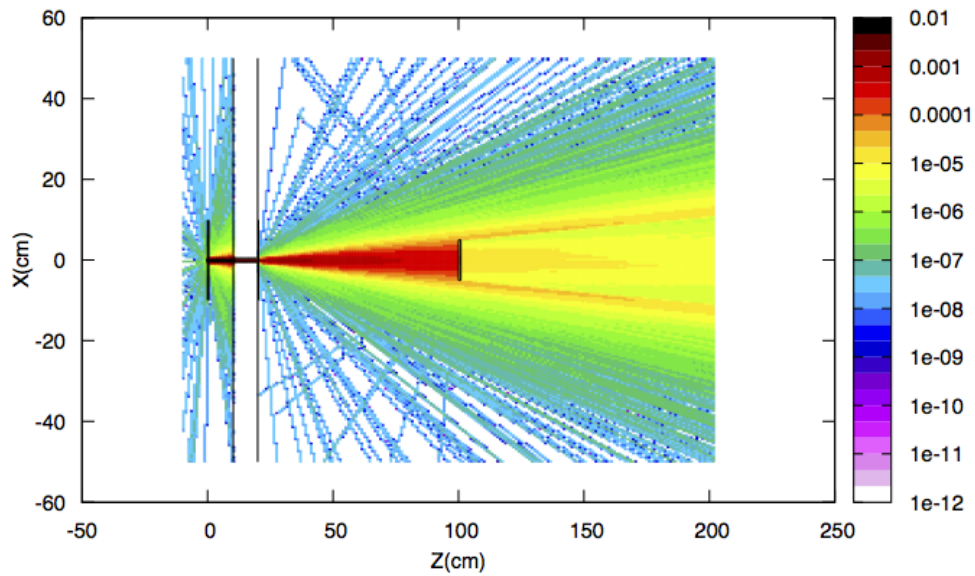
Figure 3.18: After the foils and collimator, simulation of the fluence of beam particles. Generated by using FLUKA.
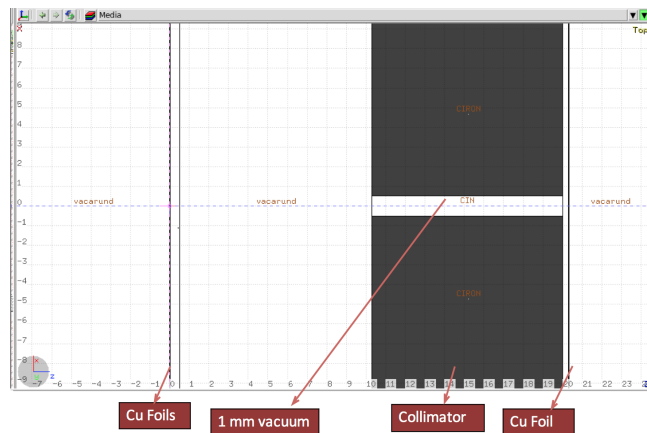
Figure 3.19: Screenshot for foils and a collimator. Generated by using FLUKA.

Melting point of Cu is approximately 1357 K which means that foils can melt after being exposed to irradiation for 5 minutes. For this reason, foils need a suitable cooling system.

After the irradiation area, the beam is planned to be stopped using an Al dump. Figure 3.21 shows the Al dump energy deposition in units of GeV/cm^3·primary. The dump

Figure 3.20: Secondary particles fluence. Generated by using FLUKA.

is placed at 165 cm on the z axis with dimensions $60 \times 60 \times 20 \ cm^3$. The Si detector is placed at the origin with dimensions $40 \times 30 \times 30 \ cm^3$. The beam line starts at 30 cm on z axis 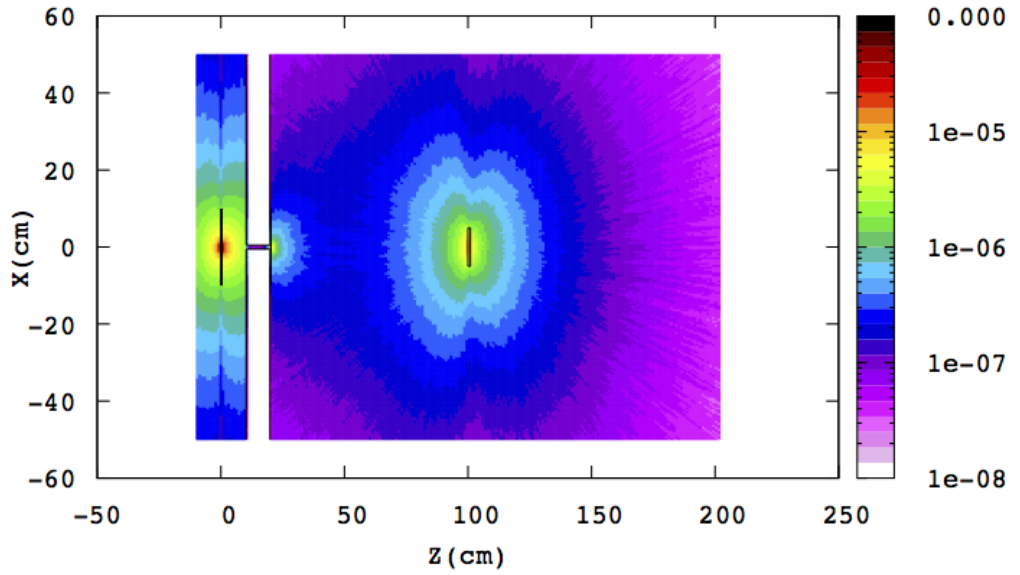going right. The small red square on the surface in the middle of the dump corresponds to stopping beam particles. Using Equation 3.1, temperature difference is found to be 12.82 K/p/s. Aluminum also needs cooling system due to its melting point being at 933.7 K.

The temperature increase calculations can be compared with the energy deposition from FLUKA using a normalization factor. This factor is calculated according to the Equation 3.2. FLUKA gives energy depositions in units of GeV/cm^3. Density of Al is 2.7 g/cm^3 and its heat capacity is 0.89 J/g·K. If all values are put into Equation 3.2, normalization factor is 4950 K·GeV/s.

$$\Delta T = \frac{\Delta E}{\rho \cdot c} \tag{3.2}$$

Figure 3.22 shows temperature increase for Al dump. The figure shows approxi-

43
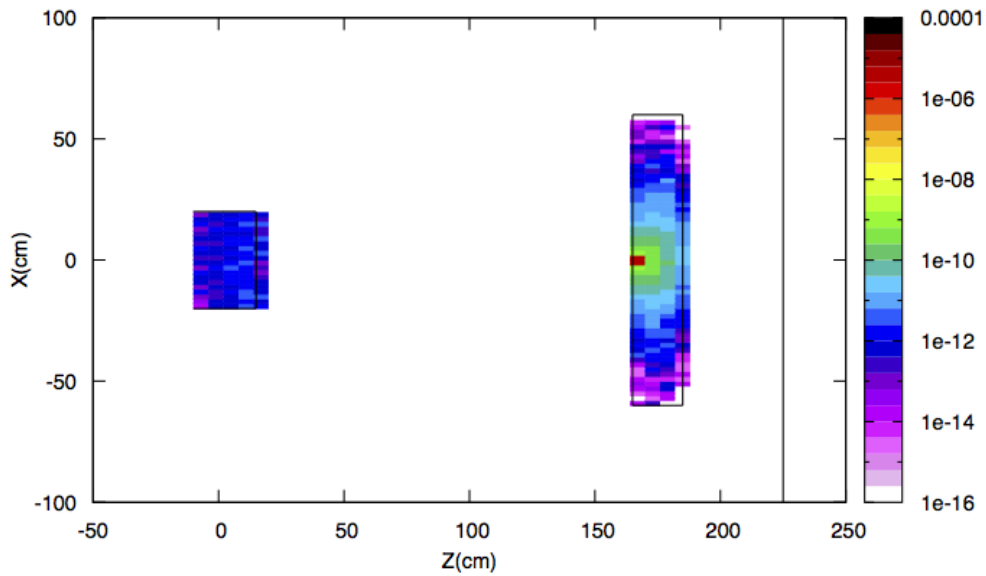
Figure 3.21: Energy deposition for Al dump after 30 MeV protons. Generated by using FLUKA.

mately 10 K/p/s temperature increase on the surface in the middle. Calculation and FLUKA simulation are compatible with each other.

According to FLUKA simulations, using Cu foils of $150\mu m$ thickness help lessen the number of particles; collimator also provides killing secondary particles. Instead of adding more foils, an additional collimator can be considered to irradiate electronic components without much energy loss of primary particles.

3.2.2   Complete Beam Line Design

Complete beam line design includes two dipole magnets, six quadrupole magnets, two Cu foils and a collimator. Whether it is suitable to use a collimator and foils or not was discussed in the former subsection. Beam line size is planned to be 21 cm after all magnets, foils and collimator. Quadrupole coefficients, location of magnets and the magnetic field values was taken from the MADX program. FLUKA and MADX design should be compatible with each other, when the design is completed.
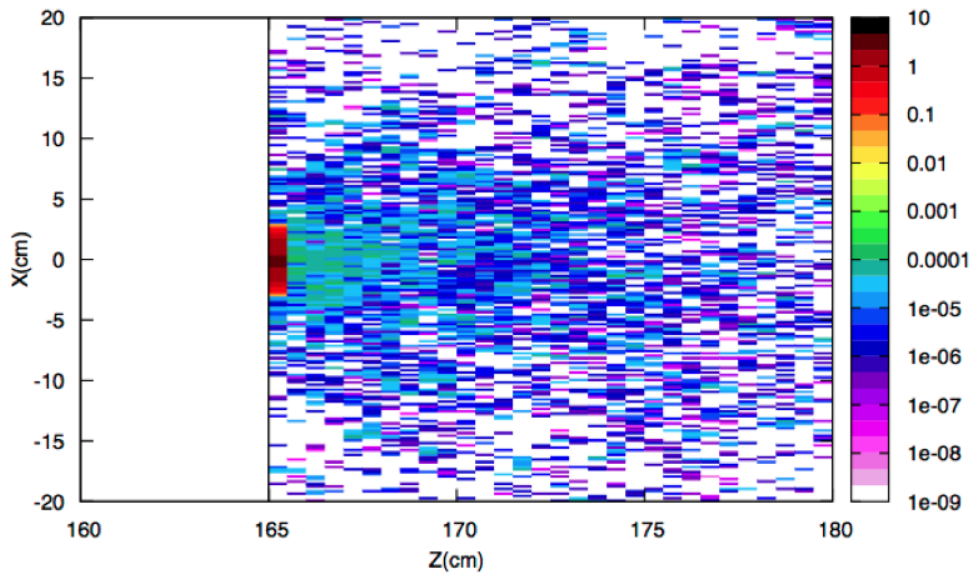
Figure 3.22: Dump temperature change. Generated by using FLUKA.

Figure 3.23 shows the trajectory of the beam line traveling in vacuum after all magnets and hitting the detector. The first and the sixth magnets are dipole magnets, the others are quadrupole magnets. All magnets consist of iron and the region of identified magnetic field is vacuum. They have to be transformed according to z axis with respect to beam line direction in FLUKA simulation.

Table 3.5 shows the magnetic field value, the length of magnets and the half aperture (H.A) of the magnet. As can be seen in Figure 3.23, while beam line particles are coming -10 cm on z axis, the first dipole helps bend them. As the beam continuning on x-z axis after the dipoles, the quadrupole magnets help expand the beam. The figure shows only the beam direction.

The beam line design using FLUKA simulation is in a preliminary design stage. The code will be improved to expand the beam size and to get the exact geometry with foils and a collimator.
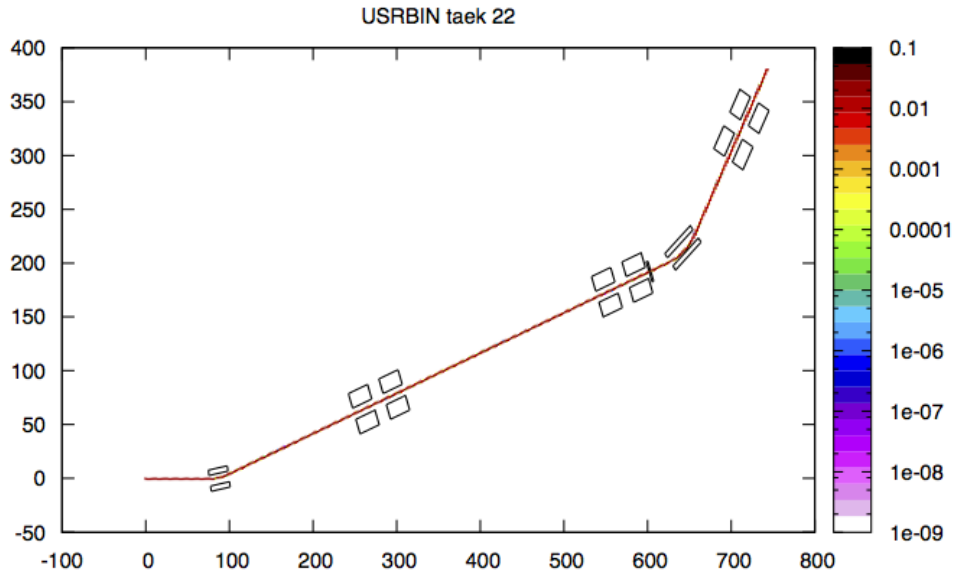
Figure 3.23: Direction of beam line after dipole and quadrupole magnets in vacuum.
Generated by using FLUKA.

Table 3.5: Beam Line Design Parameters

	Magnetic Field(Tesla)	Length of magnets(cm)	H.A-x(cm)	H.A-y(cm)
1st dipole	1.243	23	1	1
1st quad	0.045	24.4	5.5	5.5
2nd quad	-0.101	24.4	5.5	5.5
3rd quad	0.043	24.4	5.5	5.5
4^{rt} quad	-0.061	24.4	5.5	5.5
2nd dipole	1.392	40	2.3	2.3
5th quad	-0.059	24.4	5.5	5.5
6th quad	0.241	24.4	5.5	5.5

CHAPTER 4

CONCLUSION

In this thesis, radiation environment and its effects, interaction of particles with matter and SEE radiation test laboratory design was studied. In order to prevent data corruptions and fatal damage to electronic components of satellites, it is important to have an understanding of the radiation environment and resulting radiation effects.

In this thesis, single event test laboratory design is planned using 30 MeV protons in TAEK at SANAEM. This design is studied according to ESA/SCC 25100 radiation test standard. According to the standard, the flux value of PAF has to be decreased 1/2000 times. For this reason, a design for SEE radiation test laboratory simulation is studied using dipole and quadrupole magnets, Cu foils and a collimator.

This laboratory design was studied using FLUKA simulations. The preliminary beam line design shows that using Cu foils and a collimator decrease the number of particles with minimum amount of energy loss. This result is an important step in the design. MADX design also show that the beam line can be expanded using dipole and quadrupole magnets. All studies included in this thesis are currently a proof of principle.

The complete beam line design can still be improved as future work. Temperature increase simulation for the foils, the beam size simulation and dose calculations will be examined as well. Simulations can be examined to get the perfect geometry, to learn the exact beam size and to calculate the temperature difference for the necessery cooling system.

When the design is completed, the laboratory will be the first SEE radiation test lab-

oratory in Turkey.

REFERENCES

[1] O. Amutkan. *Space radiation Environment and Radiation Hardness Assurance Tests of Electronic Components to be used in Space Missions*. PhD thesis, Middle East Technical University, 2010.

[2] R.C. Baumann. Radiation induced soft errors in advance semiconductor technology. *IEEE Transactions on Device and Materials Reliability*, 5:305–316, 2005.

[3] J. et al. Beringer. Review of Particle Physics (RPP). *Phys.Rev.*, D86:010001, 2012.

[4] D. J. Bird. Study of broad-scale anisotropy of cosmic-ray arrival directions from 10^{17} to 10^{20} electron volts from fly's eye data. *The Astrophysical Journal*, 511:739, 1999.

[5] Xapsos M Bourdarie S. The near-earth space radiation environment. *IEEE TRANS NUCL SCI*, 55:1810–1832, 2007.

[6] NASA NSSDC Master Catalog. Proton satellite. `http://www.russianspaceweb.com/proton_inmarsat5f1.htm`, last visited on January 2014.

[7] CERN. Geant4. `http://geant4.web.cern.ch/geant4/`, last visited on January 2014.

[8] CERN. Transport. `http://aea.web.psi.ch/Urs_Rohrer/MyFtp/CERN-80-04/cern-80-04.htm` last visited on January 2014.

[9] M.A. Clemens. *Energy Deposition Mechanism for Proton and Neutron-Induced Single Event Upsets In Modern Electronic Components*. PhD thesis, Graduate School of Vanderbilt University, 2012.

[10] A. J. Dessler and Robert Karplus. Some properties of the van allen radiation. *Phys. Rev. Lett.*, 4:271–274, 1960.

[11] ESA. *List of Radiation Hardness Assurance Related Documents*.

[12] ESA. Spenvis. `http://www.test.org/doe/` last visited on January 2014.

[13] G. Esposito. *Study of Cosmic Ray fluxes in the Low Earth Orbit (LEO) observed with the AMS experiment*. PhD thesis, Universita Degli Studi Di Perugia, 2002.

[14] A. Ferrari et al. *FLUKA: a multi particle transport code*, 2005.

[15] B. Demirköz et al. Proposal for an irradiation facility at the taek sanaem proton accelerator facility. *Nuclear Instruments and Methods in Physics Research Section A: Accelerators, Spectrometers, Detectors and Associated Equipment*, 730(0):232 – 234, 2013.

[16] C. Balch et al. Halloween space weather storms of 2003. Technical report, Space Environment Center, 2004.

[17] C.O Hines et al. *Physics of the Earth's Upper Atmosphere*. Prentice-Hall, Inc, 1965.

[18] D.C. Carey et al. *Third order TRANSPORT with MAD input: a Computer Program for Designing Charged Particle beam Transport System*, 1980.

[19] J. R. Schwank et al. Radiation hardness assurance testing of microelectronic devices and integrated circuit: Radiation environments, physical mechanism, and foundations for hardness assurance. Technical report, Sandia National Laboratories, 2008.

[20] M. Aguilar et al. The alpha magnetic spectrometer (ams) on the international space station part i results from the test flight on the space shuttle. *Physics Reports*, 366(6):331 – 405, 2002.

[21] P. Auger et. al. Extensive cosmic-ray showers. *Rev. Mod. Phys.*, 11:288–291, 1939.

[22] The Alpha Magnetic Spectrometer Experiment. Ams-02. `http://www.ams02.org/what-is-ams/` last visited on January 2014.

[23] ENRICO Fermi. On the origin of the cosmic radiation. *Phys. Rev.*, 75:1169–1174, 1949.

[24] W. A. Hanlon. *The Energy Spectrum of Ultra High Energy Cosmic Rays Measured By The High Resolution Fly's Eye Observatory in Stereoscopic Mode.* PhD thesis, University of Utah, 2008.

[25] W. R. Leo. *Techniques for Nuclear and Particle Physics Experiments A how-to Approach*. Springer-Verlag, 1987.

[26] M. S. Longair. *High Energy Astrophysics Vol.1: Particles, Photons and Their Detection*. Cambridge University Press, 1992.

[27] R. Lozeva. *A New Developed Calorimeter Telescope For Identification of Relativistic Heavy Ion Reaction Channels*. PhD thesis, University of Sofia, St, 2004.

[28] NASA. Hubble telescope. `http://hubblesite.org/the_telescope/hubble_essentials/`,last visited on January 2014.

[29] NASA. International space station. `http://www.nasa.gov/mission_pages/station/main/#.UtZrgPRdWSo/`, last visited on January 2014.

[30] NCKU. Leap micro satellite. `http://gnss2010.ncku.edu.tw/LEAP.htm`, last visited on January 2014.

[31] Committee on Solar and Space Physics. *Radiation and the International Space Station*. NATIONAL ACADEMY PRESS, 2000.

[32] T. D. Sabino. Radiation environment and effects in human spaceflight: A lunar mission. Master's thesis, Engenharia Fisica e Tecnologica, 2012.

[33] S. P. Swordy. The energy spectra and anisotropies of cosmic rays. , 99:85–94, 2001.

[34] TAEK. *TAEK SANAEM, Proton Accelerator Facility Booklet*, 2012.

[35] TAI. Gokturk 2 satellite. `https://www.tai.com.tr/en/project/gokturk-2` last visited on January 2014.

[36] T. Tegami. *LET measurements with a Liquid Ionization Chamber*. PhD thesis, Ruprto-Carola University of Heidelberg, Germany, 2013.

[37] Liam Tung. Computer glitch caused qantas drop. `http://www.zdnet.com/computer-glitch-caused-qantas-drop-1339295336/`, last visited on January 2014.

[38] T. Wang. *Study of Single Event Transient Effects on Analog Circuits*. PhD thesis, University of Saskatchewan, 2011.